

Modeling Surface Photosynthetic Active Radiation in Taylor Valley, McMurdo Dry Valleys, Antarctica

BY

DIMITRI RICARDO ACOSTA
B.A. Northwestern University, 2005

THESIS

Submitted as partial fulfillment of the requirements
for the degree of Master of Science
in Earth and Environmental Sciences
in the Graduate College of the
University of Illinois at Chicago, 2016

Chicago, Illinois

Defense Committee:

Max Berkelhammer, Chair, Earth and Environmental Science
Peter Doran, Advisor, Louisiana State University
Andrew Dombard, Earth and Environmental Science

This thesis is dedicated to my wife, Shauna Leigh Acosta, who fed me when I was too busy to eat, got me to lay down when overdue for sleep, out of the house when I had become a hermit, kept me going when I was ready to quit, and stood by me when I was at the end of the world. Without her, the last 13.82 billion years that brought us to this very exact moment would have been a terrible bore.

ACKNOWLEDGEMENTS

Dimitri Acosta received generous support from Mexico's Consejo Nacional de Ciencia y Tecnología (CONACYT), the University of Illinois at Chicago's Department of Earth and Environmental Science, and Louisiana State University's Department of Geology and Geophysics. This work was funded by the National Science Foundation LTER grant 1115245. We acknowledge the support of the 2014/15 and 2015/16 C-511, C-505, C-506 field teams and all science support personnel that made this work possible. We would like to thank specifically Rae Spain and Renee Nofke.

DRA

TABLE OF CONTENTS

1. INTRODUCTION.....	1
1.1. Study area: The McMurdo Dry Valleys	3
1.2. Controls on radiation.....	5
1.3. Cloud cover and optical thickness.....	9
2. CASE STUDIES: RADIATION MODELING IN THE MDVS.....	11
2.1. Dana et al. 1998	11
2.2. Hoffman et al. 2008	12
3. METHODS	14
3.1. Geographical Information System	14
3.2. Meteorological record statistical analysis	22
3.3. Estimating cloud cover from meteorological data	25
3.4. Ground-truth measurements	26
4. RESULTS AND DISCUSSION	31
4.1. Met estimated seasonal potential surface PAR	31
4.2. Measured diffuse fraction of global PAR	34
4.3. Modeled cloud cover in the Dry Valleys	36
4.4. Point T-sPAR	39
4.5. Area T-sPAR.....	42
4.6. T-sPAR Toolbox	49
5. CONCLUSIONS.....	52
APPENDICES.....	56
APPENDIX A.....	56
APPENDIX B	67
CITED LITERATURE	73
VITA	78

LIST OF TABLES

TABLE I. SURFACE AREA CHANGE BY LAKE.	16
TABLE II. T-SPAR COMPUTATION PARAMETERS USED TO ESTIMATE SURFACE PAR BY POINT AND AREA FOR THE TAYLOR VALLEY BASIN.	21
TABLE III. EXPECTED INSTANTANEOUS, TOTAL DAILY AND TOTAL SEASONAL PAR FOR THE SUMMER SOLSTICE CALCULATED FROM DATA AVERAGES RECORDED BETWEEN 1996 AND 2015 BY MET LOCATION.....	33
TABLE IV. MEASURED TOTAL DAILY PAR (MOL PHOTONS M ⁻²) VS. EXPECTED TOTAL DAILY PAR FOR DAYS WITH HEAVY CLOUD COVER AND SNOW.....	36
TABLE V. SUMMARY STATISTICS FOR SEASONAL CLOUD COVERAGE NEAR MET STATION BASED ON PAR DATA.	37
TABLE VI. TAYLOR VALLEY MET STATION PREDICTIONS FOR THE SUMMER SOLSTICE (SS) AND TOTAL SEASONAL SURFACE PAR ESTIMATED USING POINT T-SPAR.....	40
TABLE VII. SUMMARY STATISTICS FOR TOTAL ANNUAL SURFACE PAR ESTIMATED BY AREA T-SPAR.	47

LIST OF FIGURES

FIG. 1. LOCATION OF THE MCMURDO DRY VALLEYS AND THE AREA OF STUDY... 4	4
FIG. 2. SOURCES OF ILLUMINATION ON A SURFACE..... 7	7
FIG. 3. HOEM MET STATION POINT RADIATION HEMISPHERICAL MAPS FOR THE AUSTRAL SUMMER. 18	18
FIG. 4. SEASONAL DISTRIBUTION OF SOLAR ELEVATION (SE) IN TAYLOR VALLEY. BARS COLORED FOR DISTINCTION. 19	19
FIG. 5. LI-1400 LI-COR HANDHELD DATA LOGGER AND LI-190 LI-COR QUANTUM SENSOR USED TO COLLECT FIELD MEASUREMENTS..... 27	27
FIG. 6. ONSET HOBO SENSOR AND SENSOR MOUNT DEPLOYED AT WEST LOBE BONNEY..... 28	28
FIG. 7. LOCATION OF ONSET HOBO AND LI-COR PAR SENSOR DEPLOYMENT BY LAKE BASIN..... 30	30
FIG. 8. LOESS BEST FIT CURVE FOR DAILY MAXIMUMS OBSERVED AT EXEM MET STATION..... 32	32
FIG. 9. MEASURED PAR AT FRLM AND HOEM MET STATIONS OVER AN 8 DAY PERIOD BETWEEN 12/30/2013 AND 01/06/2014. 35	35
FIG. 10. MODELED FREQUENCY OF CLOUD COVER BY METEOROLOGICAL STATION..... 38	38
FIG. 11. SURFACE PAR MEASURED WITH HOBO PENDANT LIGHT SENSORS PLOTTED AGAINST POINT T-SPAR ESTIMATES. 41	41
FIG. 12. TOTAL ANNUAL SURFACE PAR MAP FOR THE TAYLOR VALLEY BASIN ESTIMATED USING THE AREA T-SPAR MODEL..... 43	43
FIG. 13. TOTAL ANNUAL SURFACE PAR BY LAKE SURFACE ESTIMATED USING THE AREA T-SPAR MODEL..... 45	45
FIG. 14. BI-MONTHLY SURFACE PAR DISTRIBUTION MAPS COVERING A SIX WEEK PERIOD BETWEEN OCT 6 TH AND NOV 16 TH 48	48
FIG. 15. SURFACE PAR MAP WITH AN INTERPOLATED CLOUD COVER CORRECTION FOR A HYPOTHETICAL DECEMBER 19 TH CREATED WITH THE AREA T-SPAR TOOLBOX..... 51	51

LIST OF ABBREVIATIONS

ARIMA	Autoregressive Integrated Moving Average
BOYM	Lake Bonney Meteorological Station
CC	Cloud Cover
CSV	Comma Space Value File
D	Atmospheric Diffuse Component
DEM	Digital Elevation Model
DJF	December, January, February
EXEM	Explorer's Cove Meteorological Station
FRLM	Lake Fryxell Meteorological Station
GIS	Geographic Information System
GOES	Geostationary Operational Environmental Satellite
GUI	Graphic User Interface
HOEM	Lake Hoare Meteorological Station
IDW	Inverse Distance Weighting
JD	Julian Day
JJA	June, July, August
LOESS	Locally Weighted Regression
LWR	Long Wave Radiation
MCM LTER	McMurdo Long-Term Ecological Research Network
MDVs	McMurdo Dry Valleys
NPP	Net Primary Productivity
PAR	Photosynthetic Active Radiation
PCS	Projected Coordinate System
RMSD	Root Mean Standard Deviation
SE	Solar Elevation
SS	Summer Solstice
SVF	Sky View Factor
SWR	Short Wave Radiation
SZA	Solar Zenith Angle
T	Atmospheric Transmittivity
TIN	Triangulated Irregular Network
T-sPAR	Topographic Surface Photosynthetic Active Radiation Model

SUMMARY

Understanding primary productivity is a core research area of the National Science Foundation's Long-Term Ecological Research Network. This study maps surface Photosynthetically Active Radiation (PAR) using long term data collected by a meteorological network in the McMurdo Dry Valleys. Four stations with ≈ 20 years of records were used to correct T-sPAR, a topographic surface PAR model. Maximum expected daily surface PAR at meteorological stations was calculated for Taylor Valley, through statistical analysis of location records using a local regression model that included 84% of all observations. Expected values represent daily surface PAR under cloudless conditions. Daily measured and expected PAR was used to model cloud coverage at each location, corroborating that overcast conditions are positively correlated with proximity to the ocean. Ground-truth data collected for Taylor Valley's major lakes during the 2015/2016 field season were used to validate T-sPAR estimates. The final model approximates total seasonal surface PAR for the Taylor Valley basin. Bi-monthly maps estimate total surface PAR by lake to assist in future sampling site selection. Finally, a user interface was developed to estimate total daily surface PAR by coordinate or surface based on a user input date.

Key Words: ice-covered lakes, geographical information system (GIS), R model, meteorological data, digital elevation model (DEM)

1. INTRODUCTION

Solar radiation is a primary driving force for hydrological and biological systems across the planet. Broadly speaking, radiation is classified as either Short Wave Radiation (SWR; <700 nm, including the visible spectrum, ultraviolet, X-rays and Gamma rays) or Long Wave Radiation (LWR; >700 nm, including Infrared, Microwaves and Radio waves). Most of the incoming or downwelling radiation that reaches the planet's surface is in the form of SWR, while most outgoing or upwelling radiation is in the form of LWR (Lutgens *et al.* 2012).

The spectrum of visible light occupies a narrow waveband within SWR between 400 nm to 700 nm. This waveband of electromagnetic frequencies coincides with Photosynthetically Active Radiation (PAR), which is harnessed by photoautotrophs (cyanobacteria or plants) for primary production. The amount of radiation that actually reaches the Earth's surface, however, is not constant and is modulated by complex interactions with the atmosphere, which absorbs or scatters this energy. Understanding the spatial variability of downwelling radiation is critical in developing accurate models for heat budget, net primary productivity (NPP), hydrology and climatology (Mizoguchi *et al.* 2013).

The Antarctic continent is a unique place to study the role of SWR and PAR due to continuous 24 hours of light during the austral summer and complete darkness during the austral winter. The McMurdo Dry Valleys (MDVs) are of particular interest because the availability of liquid water beneath perennially ice-covered lakes provides an oasis for life in one of the harshest environments on the planet (Fountain *et al.* 1999). In these largely ice and snow free valleys, solar radiation is directly responsible for air and surface temperatures, the sublimation of ice and melting of the surrounding glaciers that recharge lakes (Lyons *et al.* 2000).

The MDVs have some of the lowest precipitation rates observed on the planet. Annual values range between 3 and 50 mm of water equivalent. The cause of this unique climate is the orographic precipitation shadow cast by the Trans-Antarctic Mountains (Fountain *et al.* 2009). Consequently, glacial meltwaters are the principal source of moisture in the region. This is of importance as the availability and distribution of liquid water has been identified as a limiting condition for life (Kennedy 1993, Smith *et al.* 2010, Poage *et al.* 2008). Despite this, microbial communities thrive in the active layer of the MDVs' permafrost, their productivity mediated by solar radiation's control over soil moisture (Smith *et al.* 2010).

The McMurdo Long-Term Ecological Research (MCM LTER) site maintains an array of meteorological stations that record climate variables (soil and air temperatures, downwelling and upwelling radiation, surface albedo, wind speed, and barometric pressure), for which records are available dating back to the 1993-1994 field season (Doran *et al.*, 1995). Downwelling solar radiation data, collected using pyranometers in this array, were used to develop a Topographic Radiation Model that mapped solar flux in the MDVs (Dana *et al.* 1996). More recently, a model that spatially interpolates meteorological observations (MicroMet – Liston & Elder 2006) was applied to Taylor Valley to estimate surface and subsurface glacial melt incorporating 11 years (1995-2006) of solar flux records (Hoffman *et al.* 2008). Neither of these models focus on the distribution of surface PAR nor do they establish constraints on net primary productivity in the MDVs. New methods in radiation modeling combined with an expanded record present a unique opportunity to improve on past models (Pons & Ninyerola 2008, Katurji *et al.* 2013, Kuipers Munneke *et al.* 2011, Zhang *et al.* 2013, Aguilar *et al.* 2010).

This study presents the development of a topographic surface PAR (T-sPAR) model that incorporates meteorological station observations from Taylor Valley. The model can incorporate

new observations as they are recorded, further improving its robustness. Mapping the distribution of PAR in Taylor Valley improves estimates of net primary productivity. This is especially true in the lakes. Current sampling of lake biology is restricted to a few locations per season due to lake ice cover and the availability of time and resources in the field. Present interpretation of these samples assume spatial homogeneity of biological processes across each lake (Obryk et al., 2014; Bielewicz et al., 2011; Hawes et al., 2014). Mapping surface PAR is the first step in constraining the heterogeneity of net primary productivity within the lakes.

1.1. Study area: The McMurdo Dry Valleys

Antarctica is an isolated landmass dominated by continental glaciers that cover 98% of its ≈ 14 million km^2 area. Strong winds and high levels of UV radiation during the Austral summer characterize Antarctica's climate. The summer months of December through February (DJF) receive continuous sunlight. Daily solar radiation during this period is equivalent to levels received along the equator (Dhaulakhandi *et al.* 1993). The lower albedo of the exposed rocky surface causes warmer summer temperatures in the MDVs compared to nearby areas covered in ice (Chinn 1993), and surface soil temperatures have been observed to reach $\approx 10^\circ\text{C}$ along the valley floor throughout the MDVs (Doran *et al.* 2008). On the other hand, the area is subject to cooler winters with respect to the rest of the continent's coastal areas (Chinn 1993). The winter months of June through August (JJA) are devoid of light, causing temperatures to drop below -40°C . Winds from the continent's interior have been observed to contribute to local warming, increasing temperatures in the MDVs between $+10^\circ$ and $+30^\circ$ C (Nylén *et al.* 2004). Mean annual valley bottom temperatures range between -14.8°C to -30.0°C (Doran *et al.* 2008).

The MDVs represent one of the most unique ecosystems on the planet. Located on the western shore of the Ross Sea, the greater MDVs have an ice free area of $\approx 4500 \text{ km}^2$, making them the single largest ice and snow free area in Antarctica (Levy 2013) (Fig. 1). Mean annual temperatures in the central MDVs are highest for Taylor Valley, followed by Wright Valley and Victoria Valley. Wind speeds are determined by proximity to the polar plateau, while humidity increases with proximity to the coast (Doran *et al.* 2002).

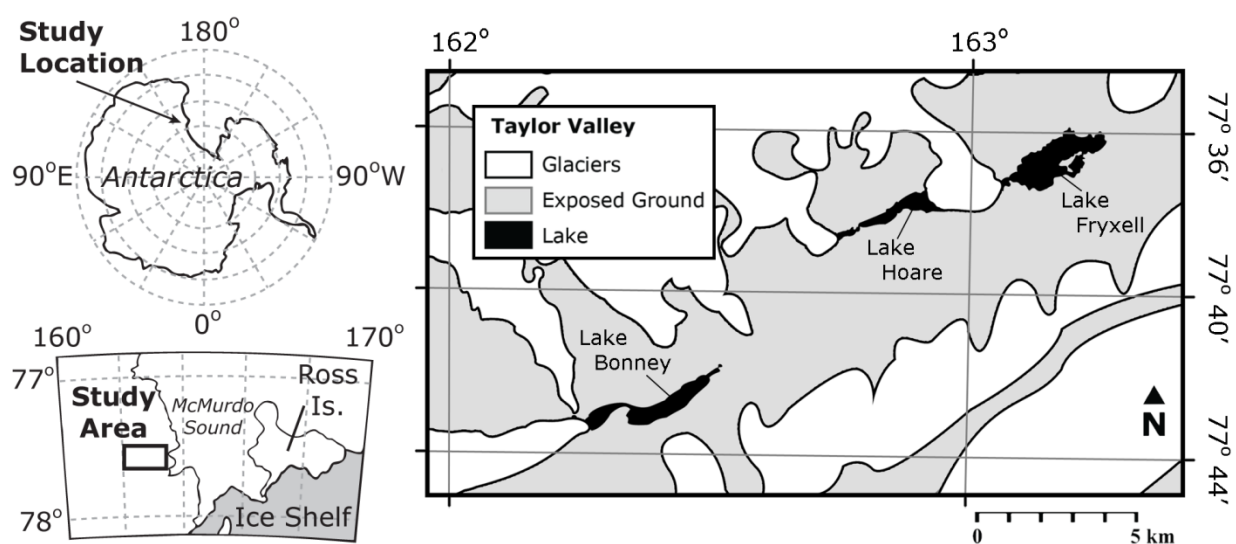


Fig. 1. Location of the McMurdo Dry Valleys and the area of study.

The presence of liquid water in the MDVs is a product of the climate history that shaped the local geomorphology. The dry valleys have been interpreted as relict fjords that rose above sea level following glacial retreat and subsequent isostatic rebound toward the end of the Pliocene (McGinnis *et al.* 1973). Glacial Lake Washburn filled Taylor Valley since the early Holocene, and is understood to have drained back out into the ocean around 7000 years ago following the recession of the Ross Ice Shelf. Between 7000 and 3000 years ago, a period of warmth allowed MDV lakes to increase in size. Cold, dry conditions followed and prevailed until 1500 to 1000

years ago when lake levels reached their minimums, some even desiccating completely (Doran et al., 1994; Wagner et al., 2011; Lyons et al., 2005; Lyons et al., 1999). The decrease in lake levels concentrated dissolved solids, permitting the lakes to remain liquid well below the freezing point of water. The climate began to warm again in the last 1000 years, increasing glacial melt and causing the remnants of the lakes to be overrun with fresh water near their surfaces. The large density gradients caused by this history prevented mixing, leading to the stratification of waters along the chemoclines that are observed today (Spigel & Priscu 1998).

1.2. Controls on radiation

All objects emit radiant energy regardless of their temperature. Radiated energy travels through the vacuum of space at a velocity of $299,792.458 \text{ km s}^{-1}$ (the speed of light). The hotter the object, the higher the frequency (and the shorter the wavelength) of the radiation it emits. Absorption of radiant energy causes molecular excitement, resulting in an overall increase in temperature. The Sun emits electromagnetic radiation across the entire spectrum including Gamma radiation. These high energy photons degrade to lower energies before they can escape into space, so outgoing solar radiation only includes frequencies greater than X-rays and ranges all the way through Radio waves (Lutgens *et al.* 2012).

Only a small portion of the total radiation emitted by the Sun reaches the surface of the Earth. Most radiation is absorbed or scattered on its way through the magnetosphere and upper atmosphere. Water vapor, suspended dust particles and atmospheric gases filter out most of the electromagnetic spectrum, allowing only some UV, most visible light, near infrared and Radio waves to pass (Mizoguchi *et al.* 2013). Assuming all atmospheric conditions are equal, the three most important modulators of downwelling solar radiation are solar zenith angle (SZA), cloud

coverage and topography (Dubayah & Rich 1995). The magnitude of radiation on a surface depends foremost on solar angle. The SZA is given to be 0° at the celestial zenith and 90° at the horizon. Alternatively, the SZA is expressed as solar elevation (SE), the complementary angle measured as the angle above the horizon. Radiation is greatest when the Sun is perpendicular to a surface such that a SZA of 0° (SE of 90°) provides maximum radiation to a horizontal surface. The spectral composition of light also varies due to changes in the ratio of direct and diffuse radiation. Diffuse radiation caused by Rayleigh scattering (the electromagnetic polarization of transparent matter) in the sky has proportionally more short wave radiation than direct radiation (causing the sky's characteristic blue color); it is however, also less intense (Dhaulakhandi *et al.* 1993).

Dubayah *et al.* (1997) identified three sources of illumination for any given point on the surface of a slope: 1) direct irradiance, 2) diffuse irradiance and 3) reflected direct and diffuse irradiance (Fig. 2). Direct irradiance is a function of the SE and is affected by optical depth (transparency of the atmosphere) and other direct obstructions such as slope shading, shadowing and sky obstruction. The SE is in itself a function of time of year, such that in the MDVs the maximum SE on the spring equinox is approximately 11.6° , while it approaches 35.8° in December on the summer solstice (ESRL - GMD n.d.). Optical depth is a function of atmospheric absorbers such as water vapor and suspended particles as well as point elevation. The influence of point elevation is due to the inverse relationship it has with pressure, which decreases along with the thickness of the atmosphere overhead and the concentration of absorbing and scattering particles. Shading is a function of the incident angle (i) of radiation on a slope, given by the equation $\cos i$, where perpendicular angles are equal to no effect whatsoever and acute angles have a detrimental effect. In contrast, shadowing is the effect of adjacent terrain

obstructing direct irradiance. In the MDVs, sky obstruction is primarily caused by terrain and cloud coverage (Dubayah & Rich 1995).

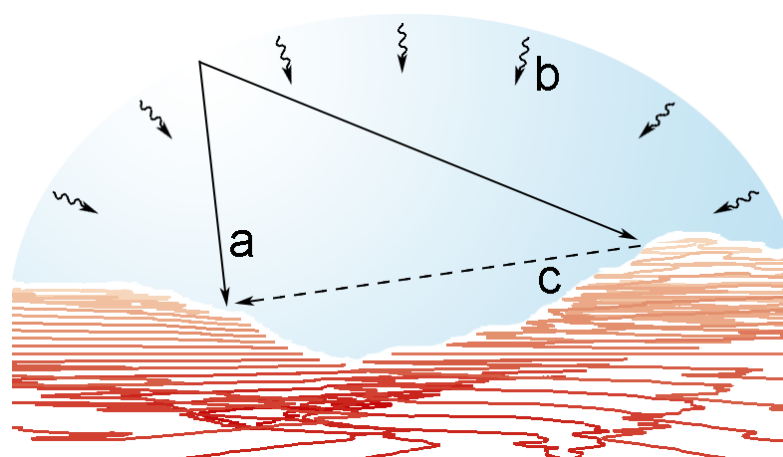


Fig. 2. Sources of illumination on a surface. Spatial variability of solar radiation has 3 main components: a. direct irradiance from the Sun; b. diffuse irradiance from the atmosphere; c. reflected diffuse and direct irradiance from nearby terrain.

Incident radiation can be estimated if the source of light is known. Predicting the position of the Sun in the sky is well understood and several methods of computing its position have been derived with varying degrees of accuracy. The basic process of calculation involves a series of trigonometric transformations to establish the ecliptic path for a terrestrial vantage point. The first step is to obtain the Julian Day Fractional Degree, a conversion of the date and time into an angle relative to a reference starting point. Next, the Solar Declination is calculated; this establishes the position of the Sun relative to the equator based on the Earth's 23.45° axial tilt. A time correction is then applied to account for variability in the ecliptic exemplified by the analemma and the Equation of Time. The Solar Hour Angle can now be established for a specified longitude (given in decimal degrees). This angle is used to determine the SZA and SE based for the coordinate latitude (also in decimal degrees). Finally the Azimuth Angle can be calculated using the latitude and SZA (Jenkins 2013, Michalsky 1988, Reda & Andreas 2008).

Diffuse irradiance cannot be calculated directly, only approximated. It is a function of the SZA, pressure/elevation and atmospheric optical depth. Atmospheric optical depth varies by latitude, generally decreasing toward the poles. The angle that radiation strikes the atmosphere must also be taken into consideration, as atmospheric scattering increases with obliquity. This effect has been incorporated into a clearness index coefficient calculated by latitude to help constrain the fraction diffuse radiation contributes toward the total (Orgill & Hollands 1977, Ruiz-Arias *et al.* 2010). Broadly speaking, the contribution of diffuse radiation toward the total on a surface is inversely proportional to cloud coverage (Liu & Jordan 1960). Furthermore, it is directionally dependent (anisotropic) and limited by the Sky View Factor (SVF). The anisotropy of diffuse irradiance can be experienced first-hand in the form of nighttime light pollution, where the sky appears brighter in the direction of metropolitan areas. The SVF is the percentage of the sky that is unobstructed from any given location on a slope. A mountain peak would have a high SVF while the bottom of a valley would have the lowest factor value (Dubayah & Rich 1995).

Reflected direct and diffuse irradiance is the most difficult illumination source to quantify. It is commonly ignored due to its small contribution to total irradiance for surfaces with average albedo. As surface reflectance increases, this source becomes more important (Dubayah & Rich 1995). Measuring average upwelling radiation for a given slope significantly simplifies the estimation of this parameter by diametrically measuring reflected direct irradiance (Dana *et al.* 1998). Reflected radiation can contribute a large fraction toward the total under certain conditions. Cloud reflection has been interpreted to cause occasional spikes in total radiation measured when cover is scattered. These conditions concentrate diffuse radiation while simultaneously permitting high incident radiation (Orgill & Hollands 1977).

1.3. Cloud cover and optical thickness

Cloud cover is the single greatest challenge to estimating solar radiation, due to its ubiquity and temporal and spatial variability. The impact on direct, diffuse and reflected irradiance varies by cloud type (thickness, water content and raindrop size distribution), base height and coverage. The density of cloud coverage has been found to cause considerable differences between radiation and absorbance/transmittance. Cloud cover is loosely subdivided into two categories: overcast or broken layers. When analyzing broken cloud layers, a further consideration is the vertical and horizontal extent of finite clouds with respect to SZA. Cloud base height can further contribute to ground-to-cloud-to-ground reflectance, especially for surfaces with high albedo. To account for this interaction, cloud base albedo can be assumed to be 50% for all clouds with bases below 5486 m (18,000 ft.) and 0% for bases greater than 5486 m. A final consideration regarding cloud coverage is the assumption that clouds will always lie between the point of observation and the Sun, which may not be the case at low SZA (Meyers & Dale 1983).

Clouds play a unique role in modulating radiation at the poles. A radiation paradox was discovered while studying light in Antarctica (Wendler 1986). For surface albedos above 60.1%, overall downwelling SWR decreases with cloudiness while LWR strongly increases. Such high albedo values are uncommon for most surfaces on Earth, but are frequently observed at high polar latitudes. This is due to the fact that dry snow has a typical albedo of 80% while wet snow is below 60%. High surface albedo triggers ground-to-cloud-to-ground reflectance. This phenomenon was observed by Dhaulakhandi et al. (1993), who noted that due to low SZA, the radiation intensity under overcast conditions was 63% less than under clear skies.

Near ground sky obstructions should also be taken into consideration when estimating solar radiation. In the MDVs such features would include large boulders, glacial walls and manmade objects such as buildings. These features can be modeled as topographic surfaces. This approach permits solar radiation to be estimated in the same way that would be done for any given slope. This oversimplification, however, carries inherent caveats that must be examined on a case-by-case basis due to their transient nature (Dubayah & Rich 1995).

2. CASE STUDIES: RADIATION MODELING IN THE MDVS

Few studies in the MDVs have focused on implementing topographic spatial analysis to understand broad environmental conditions. These types of studies are particularly well-suited to understanding surface processes that may constrain subsurface phenomena within the valley's ice-covered lakes, glaciers and exposed ground. Topographic models are effective tools to study the region during the time of year when it is physically impossible, and can incorporate long-term records measured by the extensive meteorological network currently in place. Examination of these models suggests areas of improvement while providing a framework in which to develop the present model.

2.1. Dana et al. 1998

A Topographic Radiation Model was developed for the MDVs from field measurements collected during the 1994-1995 field season (hereafter referred to as Dana-RM). Radiation data were collected in situ from 11 pyranometers across Taylor Valley, Wright Valley and Victoria Valley, to assist in determining energy balances across the complex terrain. Taylor Valley had the most meteorological stations with a total of eight. This included three Eppley pyranometers positioned on glaciers, and five Li-Cor pyranometers positioned mostly near lake shores. Wright Valley had two stations gathering data using Li-Cor pyranometers positioned near lake shores while Victoria Valley had only one (Dana *et al.* 1998).

The Dana-RM was based on previous research modeling of clear-sky spectral solar radiation across snow-covered mountainous terrain (Dozier 1980), and modeling solar radiation using geographical information systems (GIS) and the geostationary operational environmental

satellite (GOES) system (Dubayah & Rich 1995, Dubayah & Loechel 1997). The Dana-RM improved on past slope radiation models by taking into account radiation attenuation caused by variation in elevation, calculating slope sky view and terrain configuration, and estimating terrain reflectance. In doing so, the Dana-RM effectively accounts for the three principal sources of illumination previously identified: direct irradiance, diffuse irradiance and reflected direct and diffuse irradiance (Dubayah & Rich 1995, Dubayah & Loechel 1997). The Dana-RM found northern lakeshores receive less radiation due to topographic shading caused by the south facing slopes of the Asgard Range. Valley walls had similar discrepancies with steep north-facing slopes receiving more energy than steep south-facing slopes. Surface radiation on the horizontal lake surfaces of the valley bottom, were dependent on the SVF. In all cases, terrain variability played a major role in determining radiation patterns for all time scales (Dana *et al.* 1998).

2.2. Hoffman et al. 2008

Surface energy was estimated for Taylor Valley using a gridded meteorological model that integrated 11 years (1995 – 2006) of observations. A quasi-physical model (MicroMet - Liston & Elder 2006) was used to understand seasonal ablation rates on glacial surfaces and predict eventual streamflow within the basins. The MicroMet Model interpolates atmospheric forcing across topography, incorporating measurements for downwelling longwave and solar radiation, wind speed and direction, surface pressure, precipitation, relative humidity and air temperature, integrated over time. Time gaps are filled using an autoregressive integrated moving average (ARIMA). Variability in the spatial distribution of meteorological stations is adjusted for with a Barnes objective analysis scheme, a type of spatial inverse distance weighing (Liston & Elder 2006, Koch *et al.* 1983). The Taylor Valley MicroMet Model uses a 40 m digital elevation model

(DEM) resampled to a 250 m grid size. Relative humidity and air temperature are used to estimate cloud coverage within the grid, which in turn provides estimates on transmittivity to correct direct and diffuse radiation (Hoffman *et al.* 2008).

Measurements taken on the surface of Taylor Glacier were combined with MicroMet to determine the energy balance necessary to create surface and subsurface melt on the horizontal faces of Taylor Glacier. Modeled results were in close agreement with observations over diurnal timescales, predicting 100% of seasonal surface melt but less consistent on shorter timescales. Melt events have been observed on hourly timescales; however these do not result in major runoff. MicroMet reliably predicted surface ice temperatures and ablation rates over the 11-year observation period. The model suggested that surface melting was often accompanied by subsurface melt while the opposite scenario was not true. Sublimation was shown to be persistent year-round, while melting was restricted to the summer. Surface wind speeds appeared to be the most reliable predictor of surface melt due to suppressed heat loss from turbulent flux.

3. METHODS

The T-sPAR model was developed with the input of three primary data sources: modeling of a 30 m DEM, long-term single point weather observations, and point ground-truth measurements taken during the 2014/15 and 2015/16 field seasons. The DEM was processed using ESRI's ArcGIS suite to determine the slope and aspect of surfaces in Taylor Valley and create hill shade and surface radiation maps. These estimates represent maximum potential surface radiation under "cloudless" conditions. Long-term meteorological station measurements were used to build correction envelopes and interpolation of maximum surface PAR for each station. Ground-truth measurements consisted of deploying a network of sensors that measured surface radiation for the period of one week at each lake. These measurements were used to test further the validity of DEM predictions and calibrate for variability between met sensor discrepancies. An attenuation experiment was also conducted to measure surface PAR across a transect that transitioned from direct sunlight to topographic shading.

3.1. *Geographical Information System*

The 30-meter raster digital elevation model used in this study was made from earlier topographic maps published by the USGS and available for distribution from the MCM LTER Data repository (<http://mcm.lternet.edu/power-search/data-set>, accessed June 4, 2015). The Projected Coordinate System (PCS) of the DEM is WGS 1984 Lambert Conformal Conic, and has a pixel resolution of 30 by 30 m, an elevation range of 0 to 3199 m and a total area of 10 017 km². Additional GIS vector shape files corresponding to meteorological station locations and principal lake outlines were also obtained from the MCM LTER Data repository, and have the

same PCS as the DEM (<http://mcm.lternet.edu/power-search/data-set>, accessed June 4, 2015). All files were processed using ESRI ArcGIS version 10.3.0.4322 using the Spatial Analyst extension (ESRI 2016).

The original DEM was clipped using a rectangular polygon with an area of 1055 km² centered on Taylor Valley. This reduction in area was done to improve computational speed. This method, however, left a large area that was not pertinent to the analysis. Topographic shading within the valley is constrained by the surrounding ridgeline. Any point beyond the ridgeline will not cast a shadow within the valley. ArcMap's Hydrology toolset offers a means to accurately and reproducibly identify the ridgeline to restrict the raster size to the area of interest. The Fill tool removes anomalous basins in the DEM. The Flow Direction tool establishes the aspect of each pixel based on the path surface water would follow using a Queen's move scheme, allowing a gridded pixel to connect to its eight neighbors (ESRI 2015a). Downstream pixels have a larger number of connections while upstream pixels have less. The Basin tool identifies pixels from the Flow Direction that lack any connections upstream to establish basin divides, and groups all pixels that connect downstream into a single basin. Since all basins connect at sea level, care was taken to ensure the initial clip area did not join basins at the coast (ESRI 2015a). Finally the Raster to Polygon tool converts the basin limits encoded in the raster data to a vector shapefile to use as a clip path (see Appendix A for basin clipping flow chart). This procedure generated an area of interest of 673 km².

The original shapefiles obtained from the MCM LTER Data repository contained outdated vectors for Taylor Valley's major lakes. Lake level has risen substantially since the MCM LTER began monitoring, causing an increase in surface area for every major lake. The shape files are dated to 1970 and show substantial discrepancy in surface area when overlain over recent

satellite imagery. A suitable clear image taken by Landsat 8 on 12/19/2014 was selected as a reference to update lake boundaries (Landsat 8 2014). This image was chosen as it was early enough in the austral summer to observe lake boundaries without too much open water on the shores. Lake Fryxell had the largest increase in surface area with a 22.4% increase, followed by Lake Bonney with a 12.4% increase, while Lake Hoare only had a 10.3% increase despite gaining additional surface area from merging with Lake Chad (Table I).

Table I. Surface area change by lake. *Area given for Lake Hoare in 1970 combines the surface area with Lake Chad. The two lakes have since merged.

Year	Lake Fryxell	Lake Hoare	Lake Bonney
1970	5.570 km ²	2.058* km ²	4.033 km ²
2015	6.820 km ²	2.270 km ²	4.533 km ²
Change	+ 22.4%	+ 10.3%	+ 12.4 %

Surface solar radiation for Taylor Valley was calculated using the ArcMap's Point Solar Radiation tool and the Area Solar Radiation tool (ESRI 2016). The basic procedure used by both tools requires the calculation of global radiation ($Global_{tot}$) resulting from the sum of total direct (Dir_{tot}) and diffuse (Dif_{tot}) radiation. Direct radiation is calculated by summing all Sun map sectors defined by the user, where larger values increase resolution. Each sector is calculated as the product of predicted solar position based on observation coordinates, the solar constant of 1367 W m^{-2} (solar flux above the atmosphere), and an atmospheric transmittivity coefficient. Diffuse radiation is estimated in a similar manner by summing all sky map sectors. These sectors are the product of global normal radiation, anisotropic weighing, sky view factor (SVF) and a diffusivity coefficient (ESRI 2015b).

Point Radiation estimates are calculated using the specific geometry of a specified coordinate location within the DEM. A 360° viewshed map is constructed from the maximum angle of sky obstruction in every direction. The result is a topographically corrected horizon that is projected onto a hemispherical map representing the celestial dome. The viewshed output is similar to an upward looking photograph, and should be noted that east and west coordinates are inverted with respect to traditional downward looking map view. The viewshed can then be used as a filter overlain on the sky and Sun maps to constrain direct and diffuse radiation on the specified location (Fig. 3). Area Radiation applies this computation to every pixel contained within the DEM. Instead of producing a single value, the interpretation of each pixel's unique spatial characteristics creates a new raster image map of surface values (see Appendix A for Point and Area T-sPAR flow charts).

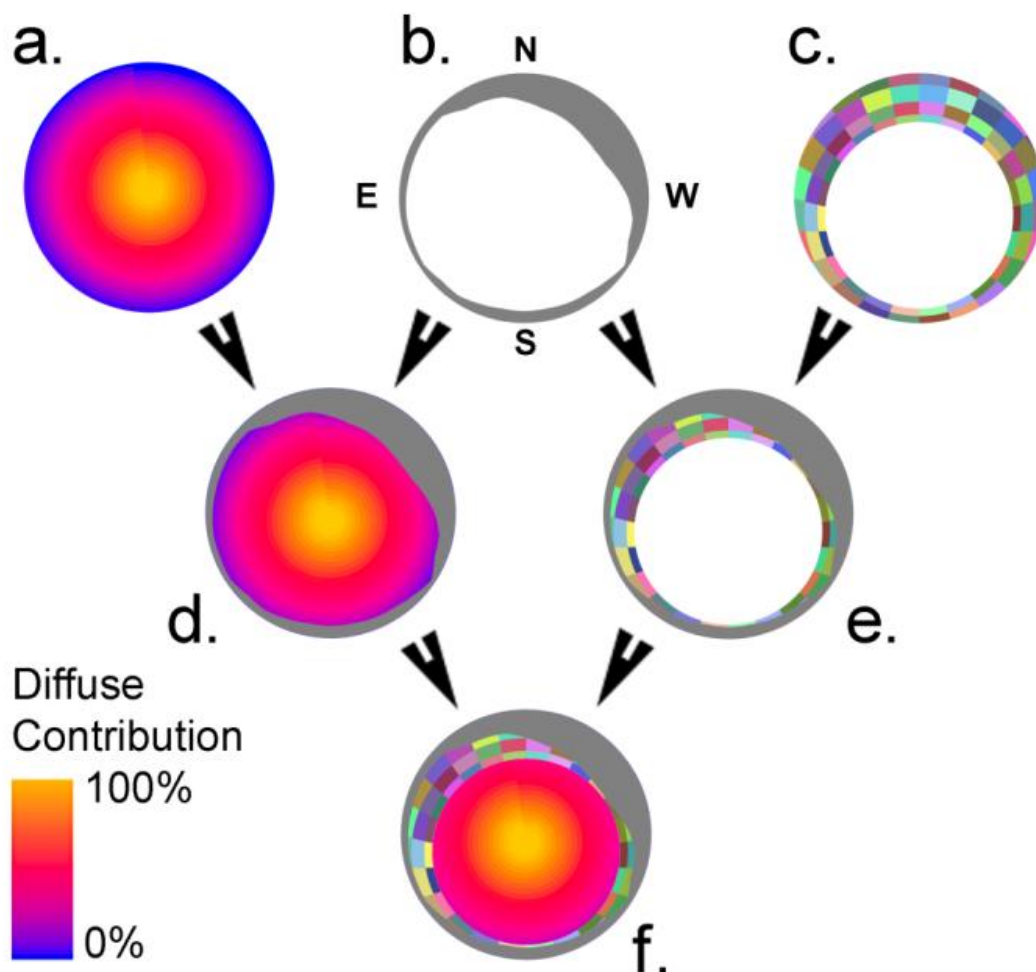


Fig. 3. HOEM met station Point Radiation hemispherical maps for the austral summer. a. Sky map: shows the area of the celestial dome that contributes the most diffuse radiation over the course of the summer. b. Viewshed: shows obstruction by Cartesian direction. The grey area represents the topographic horizon contributing shading. c. Sun map: shows solar elevations with respect to the horizon represented by sky sectors (randomly colored for contrast) used to estimate incident radiation. The concentric bands correspond to increasing solar elevation, where the innermost bands correspond to the solar path near the summer solstice. d. Sky map with Viewshed overlay: shows that the lowest hemispherical angles are completely obstructed by the topographic horizon. e. Sun map with Viewshed overlay: shows how the topographic horizon blocks sky sectors consequently obstructing incident radiation from the NW during most of the summer. f. Sky map with Sun Map and Viewshed overlay: shows interaction of all three maps with each other combined to estimate total surface radiation for that location. Note the inversion of E/W in the Cartesian coordinate system (b). The inversion applies to all hemispherical maps shown.

The often low solar angles in the Antarctic represent an obstacle to correctly modeling surface radiation. ESRI notes that special attention should be given to solar elevations below 10° due to the increase role of atmospheric diffraction (ESRI 2015b). Low solar angles result in diffuse radiation contributing a higher fraction of global radiation at the expense of decreased transmittivity. Such low solar elevations are uncommon in most of the world and represent only a small fraction of total radiation over the course of a day. However, at the latitude of the MDVs, low solar angles persist for weeks. The solar elevation in the MDVs is above 10° for only 129 days a year from mid-September through the end of March and stays below this elevation for the rest of the year (Fig. 4).

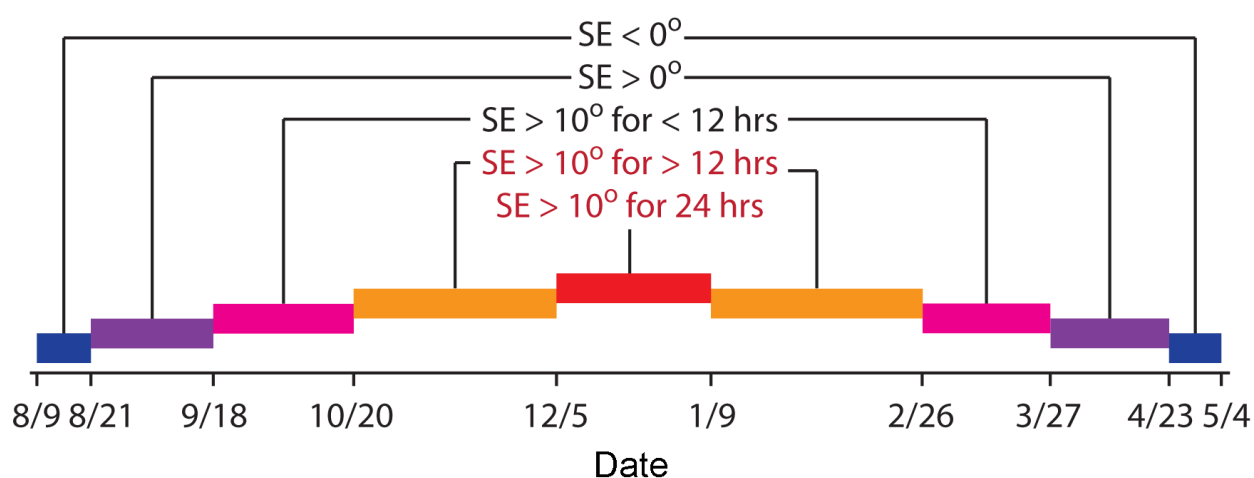


Fig. 4. Seasonal distribution of solar elevation (SE) in Taylor Valley. Bars colored for distinction. Meteorological stations record surface PAR between Aug 9th and May 4th. First and last PAR observations (SE < 0°) correspond to civil twilight when diffuse radiation accounts for 100% of global radiation. Solar angles gradually increase to 10° above the horizon (SE > 10° for < 12 hrs.) by Sep 18th for a few hours each day. The Sun stays above 10° for more than half the day (SE > 10° for > 12 hrs.) after Oct 20th. Finally it remains above 10° (SE > 10° for 24 hrs.) between Dec 5th and Jan 9th, steadily losing elevation above the horizon over the course of the following 5 months.

Parameters for estimating Area and Point Solar radiation are identical, with the sole exception that Point Radiation requires a data table with coordinates for evaluation (Table II).

Coordinates for meteorological stations as well as ground truth measurements were used to evaluate total daily point radiation to match and compare against the measured data. Different combinations of atmospheric transmittivity and diffuse components were used to find the model that predicted actual observations the best. Adjustment of these atmospheric values change surface estimates by orders of magnitude, so appropriate scaling factors were calculated for each combination by averaging the normalized value of observed over estimated predictions for the summer solstice. Finally, the root mean square deviance (RMSD) was calculated for each model iteration. Area Radiation was estimated over two week periods using the DEM model with the smallest RMSD.

Table II. T-sPAR computation parameters used to estimate surface PAR by Point and Area for the Taylor Valley basin.

Parameters	Point T-sPAR	Area T-sPAR
Input Raster	TV Basin AOI	TV Basin AOI
Input point feature or table	Met & Ground-Truth Locations	NA
Height offset	0	0
Latitude	-77.642	-77.642
Sky size / Resolution	4000	200
Time configuration	Within a day	Multiple days in a year
Start day	8/20 (JD 232)	8/20 (JD 232)
End day	4/23 (JD 113)	4/23 (JD 113)
Day interval	NA	14
Hour interval	0.25	NA
Create outputs for each interval	Y	Y
Zenith divisions	24	24
Azimuth divisions	24	24
Diffuse model type	UNIFORM_SKY	UNIFORM_SKY
Diffuse proportion	Variable 0.2-0.3	Variable 0.2-0.3
Transmittivity	Variable 0.5-0.6	Variable 0.5-0.6

ArcMap cannot calculate radiation values when the Sun is below the horizon, so estimates were computed from August 20th to April 23rd. ArcMap does not calculate solstice days correctly for time configuration settings of “multiple days in a year” or “within a day”. Values for these dates were computed using the time configuration for “special days.” ESRI documentation indicates “sky size” values over 2800 are necessary to resolve overlapping Sun maps for

temporal resolutions of 24 hours or less. A “Sky size” resolution of 4000 was tested and found to provide reliable results.

The DEM was used to estimate surface PAR over the course of the austral summer using different combinations of atmospheric transmittivity and diffuse components to find the model that predicted actual observations the best. Adjustment of these atmospheric values change surface estimates by orders of magnitude, so appropriate scaling factors were calculated for each combination by averaging the normalized value of observed over estimated predictions for the summer solstice. The diffuse fraction was varied between 0.2 and 0.3 of the global total based on reference measured estimates. Finally, the root mean square deviance (RMSD) was calculated for each model iteration.

3.2. Meteorological record statistical analysis

The MCM LTER maintains an extensive network of meteorological stations throughout the MDVs, distributed across different landscape units such as glacier surfaces, lakeshores and soil sampling locations. The current study analyzed approximately 20 years of data collected by four weather stations in Taylor Valley: Lake Bonney (BOYM), Explorer’s Cove (EXEM), Lake Fryxell (FRLM) and Lake Hoare (HOEM). These stations record PAR along with SWR, a critical secondary parameter that can be used to identify anomalous data and verify the accuracy of measurements.

Analysis of the meteorological records was performed with the statistical program R using the integrated development environment RStudio (R Core Team 2014, RStudio Team 2015). A program was written to process data downloaded from the MCM LTER Data repository (<http://mcm.lternet.edu/power-search/data-set>, accessed April 22, 2016). Observations measured

prior to the 1996/1997 field season were excluded from this analysis due to variability in the record time step. Since then, meteorological measurements have been standardized to sample every 30 seconds, and averages are recorded every 15 minutes. All four met stations used in this study have records from 1996-2015 except for EXEM, which has records from 1997-2015.

A MetAnalyst R-script was developed to assist in data anomaly detection and establish PAR measurement envelopes from meteorological observations. This script makes a copy of each station's data log file and makes some minor modifications to reduce its size, primarily removing long wave radiation data and modifying the column structure. The program then separates the copy into individual files based upon the field season year, defined as beginning after the winter solstice and ending on the winter solstice of the following year (June-June). PAR and SWR records are then recast as two separate data tables to allow cross-comparison by calendar day over time for each weather station. The minimum, mean, and maximum are calculated for every time step and for each day interval.

Daily PAR values are automatically plotted by MetAnalyst, and figures are exported to PDF format. The program generates plots for minimum, mean, and maximum daily observations over the entire record and per year to assist in anomaly detection (see Appendix B for anomaly detection methods). Linear time series facet plots of minima, mean and maxima by year, for all years, are plotted together for comparison and identification of gaps in the record. Facet Plots are also generated at higher resolution showing PAR and SWR side by side to identify the response of each sensor under local conditions. These plots help identify sensor malfunctions. PAR and SWR are plotted against each other independent of time, and a linear regression is applied with a confidence interval envelope to identify statistical outliers. Plots of PAR normalized by SWR help identify anomaly time periods.

The MetScrubber R-script removes records from the data frame based on user-specified time frames. It also sets all met observations between last and first light to zero as there should be no significant light sources in the valley during this period. Analysis of meteorological data suggests that first light is observed in the valley around August 9th. This was determined based on PAR measured at or above one $\mu\text{ mol photon m}^{-2} \text{ s}^{-1}$ for a minimum of one hour over the course of a day. Similarly, last light is observed in the valley around May 4th by the same criterion. Once anomalous observations are removed, the program generates point cloud scatter plots for daily minimum, mean, and maximum. A best fit curve for each station's data is approximated using LOESS (Locally Weighted Regression) with a smoothing parameter (α) value of 0.25. The smoothing parameter controls the number of data points included in the estimate, where large α values produce the smoothest fits and small α values conform more closely to the data (Cleveland & Devlin 1988). This value was chosen because it generated a curve that best fits the data. The LOESS best fit curve for daily maximums was used to estimate the upper confidence interval with a standard deviation (σ) = 1, equivalent to 84% of all observations. This curve represents the maximum daily PAR recorded at each weather station under *cloudless* conditions during peak radiation hours. The curves for each station are used to correct T-sPAR estimates.

PAR measurements recorded at met stations represent instantaneous values sampled every 30 seconds and averaged over 15 minutes, given in $\mu\text{ mol photons m}^{-2} \text{ s}^{-1}$. To obtain the total amount of PAR measured at the surface at each met station location, it is necessary to convert values to daily mol photons m^{-2} . The conversion to daily totals from record measurements can be calculated by the following equation:

$$\text{daily mol photons } m^{-2} = \sum_{i=m}^n \mu \text{ mol photons } m^{-2} s^{-1} * \frac{60 \text{ sec} * 15 \text{ min}}{1 \text{ min} * 10^6} , \quad (1)$$

where $n = 96$, the total number of 15 minute records in a day. Instantaneous values were converted to daily totals for every day in the record and plotted to calculate the best fit LOESS.

3.3. Estimating cloud cover from meteorological data

Estimating the extent of cloud cover (CC) over the course of a day is difficult to measure directly due to the temporal nature of clouds. Changes in atmospheric transmittivity over the course of a day can be used to approximate CC to some extent. High transmittivity throughout the day results in the highest measured values of PAR and SWR recorded at each met station. The LOESS best fit curve for total daily PAR in this case is assumed to be equal to 100% transmittivity. Any measured deviation below the total daily predicted value can be attributed to reduced atmospheric transmittivity caused by increased CC, while measured values that approximate the predicted value are the result of mostly clear conditions.

Daily CC was calculated as a percentage using the following equation:

$$CC = \left[1 - \left(\frac{\text{Measured Total Daily PAR}}{\text{Estimated Total Daily PAR}} \right) \right] \times k , \quad (2)$$

CC > 1 = 1 AND CC < 0 = 0

where k is an arbitrary constant, determined by a chosen threshold, used to constrain CC values between $0 < 1$. Examination of witnessed overcast days during the 2014/2015 and 2015/2016 field seasons suggested a 50% decrease in transmittivity equals 100% cloud cover so $k = 2$. A high CC value is equivalent to overcast conditions persisting for all or most of the day, while a

low CC value indicates sustained clear conditions. Intermediate values are necessarily more ambiguous as they could indicate scattered cloud conditions throughout the course of the whole day or high CC during peak radiation hours transitioning to clear conditions during off-peak hours.

Accurate estimation of daily CC relies on the sum total of daily measured PAR. Only records with 96 daily observations were included in this analysis. Records with fewer daily observations would be biased toward lower daily sums and inaccurately identified as days of high CC. It should be noted that values outside of the CC limits $0 < 1$ are possible since the optical thickness of cloud coverage can still vary within completely overcast days. Similarly, diffuse radiation concentration under scattered cloud conditions can result in measured values that exceed the estimated total daily value. For purposes of this analysis any value less than zero was set to zero, and any value greater than one was set to one.

3.4. Ground-truth measurements

Ground-truth measurements of surface PAR in Taylor Valley were recorded between October and December of the 2015/2016 field season. A sensor network of ten Onset HOBO Pendant Light sensors was deployed across the three major lakes of Taylor Valley for approximately one week at a time. Data were also simultaneously collected using a LI-1400 Li-Cor handheld data logger and a LI-190 Li-Cor Quantum sensor with leveling capabilities (Fig. 5). The handheld data logger and one Onset HOBO sensor were set up in close proximity to the local met station for the duration of the sample period to serve as reference controls for met station records. All pendant loggers were set to record measurements every 15 minutes while the LI-1400 was set to sample every 5 minutes and log the mean every 15 minutes.



Fig. 5. LI-1400 Li-Cor handheld data logger and LI-190 Li-Cor Quantum sensor used to collect field measurements. Logger is shown beside a handheld GPS unit in the foreground. The logger was connected to the Quantum sensor via a ≈ 3 m long cable, pictured in the background (circled to help identify).

The Onset HOBO sensors were deployed using sensor mounts of rudimentary design. Each mount consisted of a square wooden block cut from 1x4 lumber attached at the middle to a foot and a half of white canvas. The canvas was used to weigh the sensor mount down with rocks found in the field. A flat, notched wooden dowel cut to size served as the housing for the pendant's beveled underside. The pendant was secured to the mount with a rubber band and a

split ring looped through a small eyebolt affixed to the block (Fig. 6). The small light weight design made it possible to carry all mounts in a backpack and deploy them quickly once a suitable location was selected. Sensors were leveled using a small bubble bullseye.



Fig. 6. Onset HOBO sensor and sensor mount deployed at West Lobe Bonney.

A field calibration experiment was conducted with the Onset HOBO sensors to evaluate their accuracy at measuring solar flux and to test robustness of the sensor mount under the harsh Antarctic field conditions. All ten sensors were set up in close proximity to each other on a north facing slope in the Lake Bonney basin. Sensors were carefully oriented to have similar aspects. Flat rocks with a low profile and similar color were chosen to mitigate shadow effects and reflectance due to differences in albedo. The PAR sensor was placed in the center with five Onset HOBO sensors on either side. The pendant sensors ran two separate routines for three days at a time. The first routine recorded a measurement every five minutes. The second routine recorded a measurement every 15 minutes. The PAR sensor was used as a control and ran the same five-minute sample, averaged every 15 minutes in both scenarios.

The sample locations of Onset HOBO sensors were chosen with the intention of maximizing the spatial distribution of the network. Different areas were chosen both on the lake surface and on the lake shore, with an emphasis on topographic characteristics such as points within the domain of diurnal topographic shading, or alternatively free of shade when most areas were obstructed or uncommon surface ablation (Fig. 7) Sensor HB 01 was set beside the met station at all locations. All other sensors were distributed randomly.

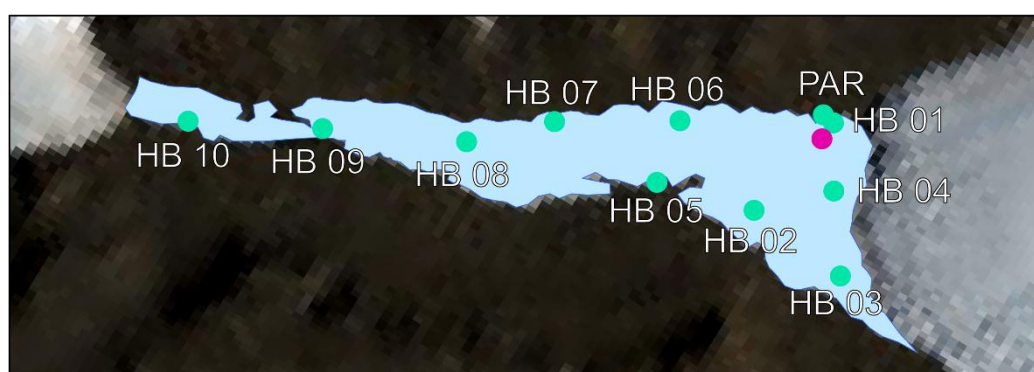
EXEM met is approximately five km east northeast of Lake Fryxell and two to three km west of McMurdo Sound. This station is not near any major ice-covered lake or glacier, a feature that makes it a useful control. The station is also at one of the widest points in Taylor Valley, so it should receive the least amount of topographic shading. Unfortunately, the field season schedule did not allow for time to measure this station with the portable PAR sensor, and was the only met station without control data. In lieu of a control, HB 02 was set up beside the station for the duration of ground-truth measurements recorded for the Lake Fryxell basin (Fig. 7).

Finally, a light attenuation experiment was conducted mid-December of the 2014/2015 field season on the northeast shore of Lake Hoare near the camp. The experiment was conducted in the late afternoon on a clear sunny day, when the Lake Hoare basin was heavily shaded by the Asgard Range to the northwest. Instantaneous measurements were taken using the Li-Cor PAR sensor, beginning in an area with full incident radiation. Measurements were then taken along the umbral horizon (boundary edge of the topographic shadow) and were then recorded moving away from the horizon for some distance. Measurements were taken behind a large boulder which limited the sky view area at that particular location. Additional measurements were taken on the return back to Lake Hoare camp, which by that time was in full sunlight. A last measurement was taken in the shadow of a large boulder adjacent to the main hut.



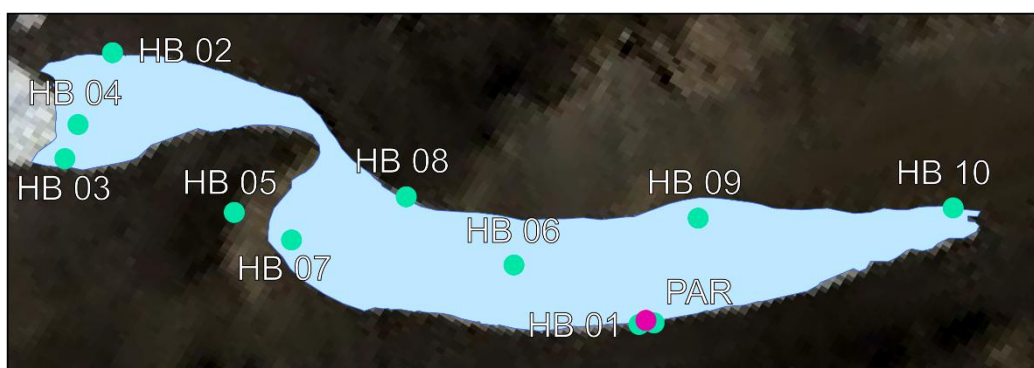
Lake Fryxell

● Met Station ● Sensor Location Lake 0 0.75 1.5 km



Lake Hoare

● Met Station ● Sensor Location Lake 0 0.5 1 km



Lake Bonney

● Met Station ● Sensor Location Lake 0 0.5 1 km

Fig. 7. Location of Onset HOBO and Li-COR PAR sensor deployment by lake basin. Control sensors were deployed beside met stations. EXEM met was sampled at the same time as Lake Fryxell. Note difference in distance scales for each map. Lakeshore boundaries are set to 12/19/2014. Landsat 7 base image obtained from the MCM LTER Data repository (<http://mcm.lternet.edu/power-search/data-set>, accessed June 4, 2015).

4. RESULTS AND DISCUSSION

4.1. Met estimated seasonal potential surface PAR

Best fit curves were found for the minimum, mean and maximum instantaneous daily values observed at each met station. A locally weighted regression (LOESS) model was used to determine the envelope of instantaneous potential surface PAR. This envelope represents the range of expected daily values. The curves themselves represent the smoothed average of the daily observations over the whole record. It is understood, however, that the absolute potential instantaneous daily maximum should be a value that is greater than the average best fit curve for the maximum. This is because such a value depends on cloudless conditions during solar noon. Any degree of reduction in transmittivity during this time period would result in values that are lower than the absolute maximum potential.

A value of one standard deviation above the best fit LOESS curve for instantaneous daily maximum observations was chosen to represent the absolute potential daily maximum. This value includes 84% of all daily maximum observations over the entire record (Fig. 8). The top 16% of observed maximum values are interpreted to be the result of concentrated diffuse radiation caused by scattered cloud reflection, as described by Orgill & Hollands (1977). This curve predicts PAR values over $\approx 1600 \mu \text{ mol photons m}^{-2} \text{ s}^{-1}$ during the height of the austral summer. Instantaneous PAR measurements recorded in the field during the 2014/2015 field season support these predictions. These values are up to $\approx 250 \mu \text{ mol photons m}^{-2} \text{ s}^{-1}$ higher than best fit LOESS curve values.

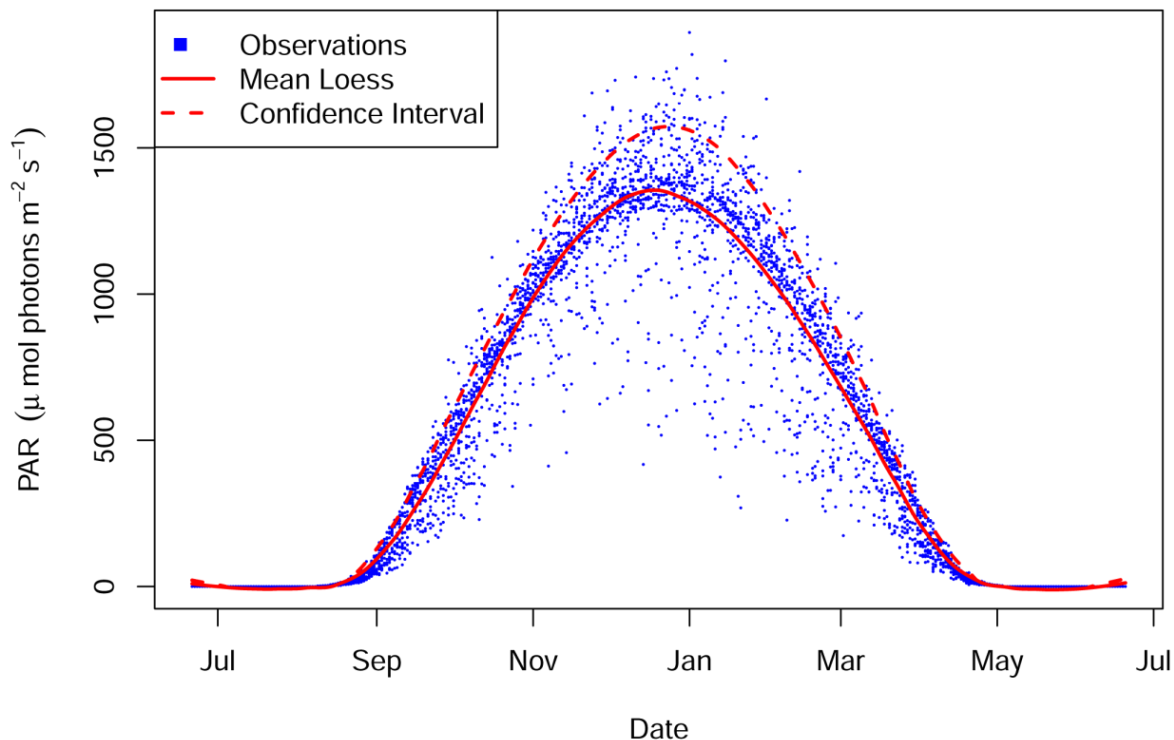


Fig. 8. LOESS best fit curve for daily maximums observed at EXEM met station. One standard deviation above the best fit curve includes 84% of all observations. The upper confidence interval curve was chosen to represent the absolute maximum seasonal potential surface PAR for records from that station.

A comparison of all LOESS envelopes shows a normal distribution of surface PAR centered on the summer solstice. All met stations receive comparable amounts of PAR during the peak of the austral summer (Table III). The Lake Bonney met station records the highest values of instantaneous surface PAR during this time, and has the largest range in expected daily values. Envelopes for FRLM and EXEM met stations are most similar to each other, and both receive intermediate amounts of surface PAR over the course of the season compared to other stations. HOEM absolute maximum, mean maximum and mean average surface PAR are the lowest with respect to all other met stations included in this study (Table III). This fact is consistent with heavy daily topographic shading in the narrow valley. Daily instantaneous maximum surface PAR values of $500 \mu \text{ mol photons m}^{-2} \text{ s}^{-1}$ are recorded at all stations by October, and double to

1000 μ mol photons $m^{-2} s^{-1}$ by November. Values above 1500 μ mol photons $m^{-2} s^{-1}$ are observed from late November through mid-January. Daily values drop below 1000 μ mol photons $m^{-2} s^{-1}$ by late February and below 500 μ mol photons $m^{-2} s^{-1}$ by mid-March.

Table III. Expected instantaneous, total daily and total seasonal PAR for the summer solstice calculated from data averages recorded between 1996 and 2015 by met location.

Instantaneous Daily PAR (μ mol photons $m^{-2} s^{-1}$)	BOYM	EXEM	FRLM	HOEM
Absolute Max	1622	1571	1598	1540
Mean Max	1375	1354	1348	1277
Mean Average	636	700	680	627
Mean Min	113	197	154	171
Total Daily PAR (mol photons m^{-2})	65.34	72.73	71.83	67.23
Total Annual PAR (mol photons m^{-2})	7584	8477	8479	6938

Total daily surface PAR was calculated for all met stations to allow comparison against GIS predicted values. Instantaneous PAR units were converted to daily mol photons m^{-2} , and 15-minute averages were summed to calculate the daily total. A best fit LOESS curve was fitted to the data for each met station, and was used to calculate the limits of the upper one standard deviation confidence interval. This interval was chosen because it appeared to fit the upper limits of daily totals for all stations without over-predicting any observations. In contrast to instantaneous daily PAR measurements, total daily surface radiation appeared to decline from east to west suggesting a correlation with total width of the valley floor and height of the surrounding ridge line. The largest daily totals were observed at EXEM met at the height of the austral summer, followed closely by FRLM met, with comparable total daily values and only slightly higher totals for the entire season (Table III). Estimates for BOYM data show higher

total seasonal values compared to HOEM. PAR values at HOEM surge above BOYM for a few weeks prior and following the summer solstice. During this period, daily solar elevation is great enough for the Sun to remain above the Kukri Hills to the south of the Lake Hoare basin. This contributes incident radiation to the area during the “evening” hours at HOEM while BOYM remains topographically shaded.

4.2. Measured diffuse and reflected fraction of global PAR

An eight-day period between 12/30/2013 and 01/06/2014 was examined to evaluate the contribution of diffuse and reflected radiation toward global radiation. This time period was chosen because observed daily maximums at both HOEM and FRLM remained relatively consistent from day to day over the interval. During this time of year, local topography shadows HOEM met between 16:00 and 16:30 hrs. while FRLM met remains in direct sunlight. Consequently, measured values at FRLM represent the sum of incident, diffuse and reflected radiation on a surface, while measured values at HOEM lack the incident fraction due to topographic obstruction.

The relative proximity of HOEM and FRLM stations to each other (≈ 6.6 km) ensured that similar weather conditions persisted at both locations. The two time series were plotted for comparison (Fig. 9) Scaling PAR measured at FRLM to match HOEM yields a predicted value for PAR for that time step of $\approx 941 \mu \text{ mol photons m}^{-2} \text{ s}^{-1}$ while the average of actual measurements in full topographic shade is $\approx 247 \mu \text{ mol photons m}^{-2} \text{ s}^{-1}$. This suggests the contribution of incident radiation to be $\approx 694 \mu \text{ mol photons m}^{-2} \text{ s}^{-1}$ or 74% of the global total. Accordingly, the diffuse and reflected contribution is equal to 26% of the total global value.

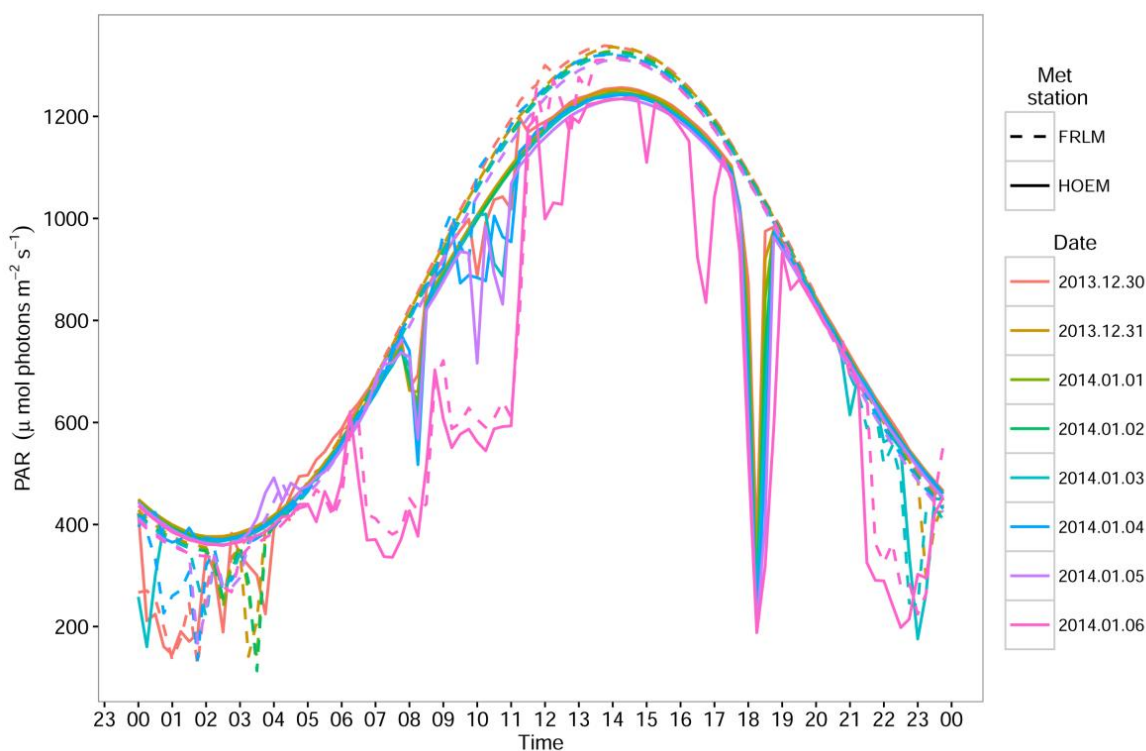


Fig. 9. Measured PAR at FRLM and HOEM met stations over an 8 day period between 12/30/2013 and 01/06/2014. During this time of year HOEM met receives daily topographic shading around 18:00 hrs. Plot shows diffuse component of PAR measured at HOEM at 18:15 is $\approx 26\%$ of the value measured at FRLM.

The attenuation experiment at Lake Hoare consisted of instantaneous measurements taken between 18:50 and 20:00 hrs. on 12/11/2014 along a transect that transitioned from full sunshine into topographic shade. Additional measurements were taken at the umbral horizon to evaluate the distance at which PAR attenuated to background diffuse radiation under topographic shading. Averaged unshaded measurements at that time were $\approx 946 \mu \text{ mol photons m}^{-2} \text{ s}^{-1}$ while the average shaded values were $\approx 144 \mu \text{ mol photons m}^{-2} \text{ s}^{-1}$, representing an incident contribution of 85% and a diffuse/reflected contribution of 15% to the total global value. Measured PAR attenuated to background diffuse values at a distance of $\approx 35 \text{ m}$ from the horizon. Surface PAR was measured up to a distance of $\approx 300 \text{ m}$ from the horizon and was not found to diverge noticeably for surfaces with comparable sky view factors.

4.3. Modeled cloud cover in the Dry Valleys

Seven overcast days were examined to identify the effect of heavy cloud cover on total daily PAR. These dates were observed to have snow events or were overcast for most of the day. Events were documented with a combination of photographs, field log book records, and secondary surface PAR measurements with the handheld device. Three events were identified during the 2014/2015 field season and four during the 2015/2016 field season. Total daily PAR was calculated for each day using meteorological records from the nearest station. These dates were compared to meteorological station records for incoming and outgoing SWR to confirm that the decrease in daily values was not caused by snow obstructing the sensor. Measured totals were compared to the expected daily values based on the upper confidence interval of the best fit total daily LOESS curve (Table IV).

Table IV. Measured total daily PAR (daily mol photons m⁻²) vs. expected total daily PAR for days with heavy cloud cover and snow.

Date	Observation Location	Snow Event	Measured daily PAR	Expected daily PAR	Percent of Total
11/18/14	Lake Bonney	N	23.83	53.93	44%
11/27/14	Lake Bonney	Y	28.59	59.19	48%
11/30/14	Lake Bonney	N	33.98	60.65	56%
10/23/15	Lake Fryxell	Y	29.91	35.18	85%
10/31/15	Lake Fryxell	Y	17.81	43.23	41%
12/06/15	Lake Fryxell	N	41.08	69.29	59%
12/08/15	Lake Fryxell	N	35.39	69.99	51%

Days with heavy cloud cover receive approximately one half of the expected daily value of PAR. The exception to this trend was the snow event that occurred on 10/23/2015. This snow event began in the evening after peak radiation hours. Close examination of the FRLM record

shows little difference compared to a cloud-free day. The only signal appreciable in the record is lower than expected values during the “night-time” hours, when solar angles are lowest and PAR values are inherently low. This event highlights the difficulty in identifying cloud coverage when solar elevation is low.

Overcast conditions were binned into four categories: clear ($0 < 0.2$), scattered ($0.2 < 0.5$), broken ($0.5 < 0.8$) and overcast ($0.8 < 1.0$). Frequency statistics were calculated for each year along with a seasonal total by met station (Table V). This analysis shows agreement with previous reports of positive correlation between cloud coverage and proximity to the ocean (Doran *et al.* 2002). Seasonal totals show that cloudiness is greatest at EXEM met, on the eastern end of Taylor Valley. This location has the highest incidence of both overcast and broken cloud conditions, accounting for up to 32% of all observations during a season. Clear conditions, on the other hand, are most common on the western end of Taylor Valley near BOYM met.

Table V. Summary statistics for seasonal cloud coverage near met station based on PAR data.

Met Location	Clear	Scattered	Broken	Overcast
EXEM	44%	23%	17%	15%
FRLM	46%	25%	15%	14%
HOEM	47%	26%	17%	10%
BOYM	53%	28%	12%	7%

The frequency of modeled observations was aggregated by month to determine if atmospheric patterns concentrate at specific times during the austral summer (Fig. 10). Results show that cloud-free, clear days predominate across Taylor Valley for most of the summer, with a slight decrease in frequency as the summer progresses. Conversely, overcast days appear to increase in frequency toward the end of the summer. The change in frequency appears well correlated between observations at BOYM, EXEM and FRLM, with all three stations reaching a

peak during the month of February. HOEM met is the only met station that shows a distinct increase in overcast conditions around the summer solstice.

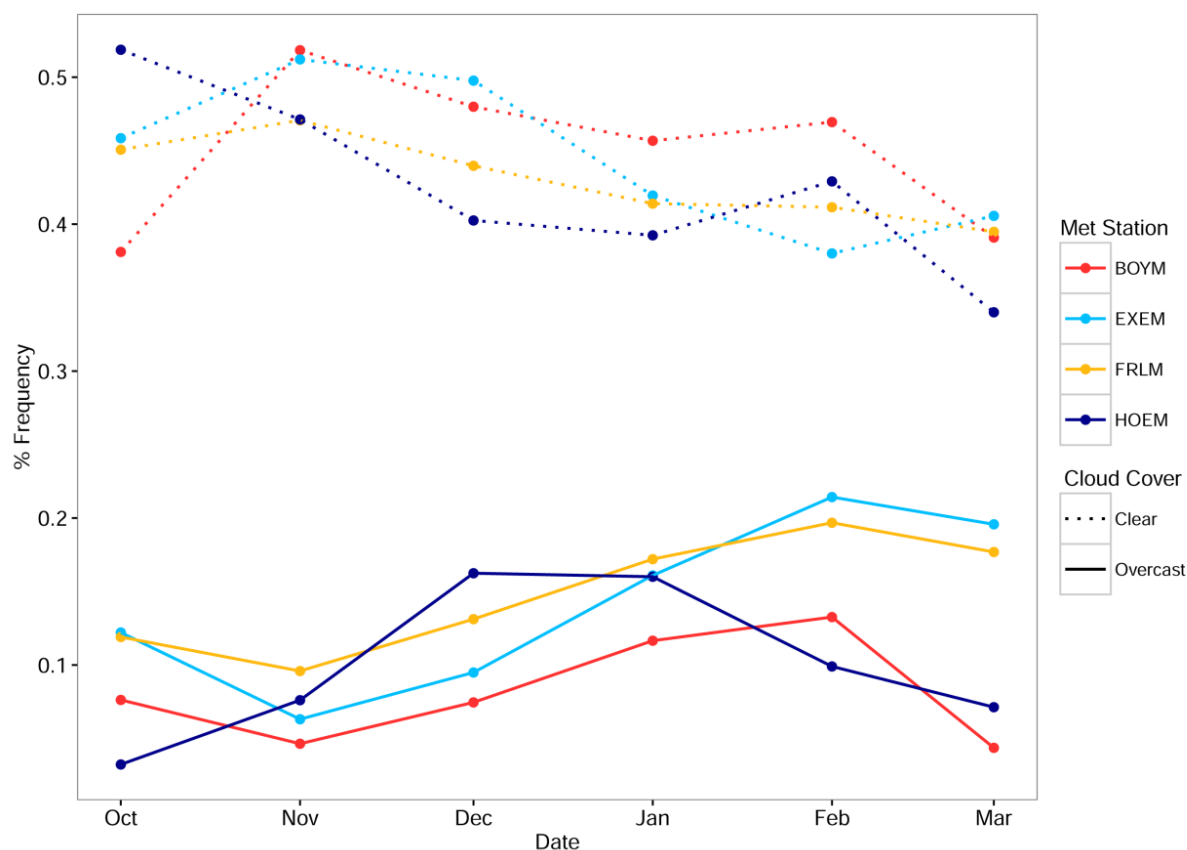


Fig. 10. Modeled frequency of cloud cover by meteorological station. Total observations are aggregated by month and displayed as a percentage of the monthly total. Only “Clear” and “Overcast” conditions are shown to improve plot readability.

Since the CC model relies on the difference between measured and expected PAR, it is difficult to determine conclusively the accuracy of frequency estimates at the beginning and end of the austral summer (Fig. 10). The low availability of radiation during the fringe months makes the difference between overcast and clear days too small for sensors to discern. Another aspect to consider is that at such low solar angles, the Sun may remain unobstructed by cloud coverage, possibly even illuminating clouds from beneath as is often observed with nacreous clouds. Under these conditions cloud coverage would contribute to an increase in surface

radiation by reflecting incident radiation downward. Given these considerations, it is recommended to limit conclusions only to estimates between October and March.

4.4. Point T-sPAR

Values for the diffuse component (D) were varied between 0.2 and 0.3 based on the measured diffuse fraction (where a value of one equals the total fraction of global radiation). Transmittivity (T) was varied between 0.5 and 0.7 (where 0.5 is the standard for clear conditions and higher values represent exceptionally clear conditions). Outputs were scaled to match the LOESS upper confidence interval. This allowed for direct comparison against met estimated total daily surface PAR and calculation of the RMSD for each model.

All Point T-sPAR estimates generally under-predict daily total surface PAR and identify HOEM met with the lowest annual total of surface PAR. The default ArcMap parameters for clear conditions (D 0.3, T 0.5) yield the largest RMSD for all met station estimates (Table VI). This model estimates total annual surface PAR to be highest at BOYM met. Decreasing the diffuse fraction while increasing atmospheric transmittance (D 0.2, T 0.5) reduces the RMSD for individual station estimates, but continues to predict the greatest radiation at BOYM met. Maintaining the diffuse fraction at default clear conditions and increasing transmittance (D 0.3, T 0.6) predicts higher surface PAR at EXEM, followed by BOYM met producing even lower RMSD. The model parameters that produce the best fit to observed values uses the standard diffuse fraction paired with high transmittance (D 0.3, T 0.7). This model predicts the highest total surface PAR at EXEM (Table VI). It continues to predict higher annual values for BOYM than FRLM, but decreases the gap between them and predicts FRLM to receive higher surface

values around the summer solstice. The model does not correctly predict the HOEM surge in surface PAR surrounding the summer solstice that is observed in actual measurements.

Table VI. Taylor Valley met station predictions for the summer solstice (SS) and total seasonal surface PAR estimated using Point T-sPAR.

Atmospheric Parameters	Point T-sPAR (daily mol photons m ⁻²)	BOYM	EXEM	FRLM	HOEM
D 0.3, T 0.5	SS Total Daily PAR	70.78	70.15	68.67	67.63
	Total Annual PAR	7196	7047	6834	6166
	RMSD	4.12	6.50	7.49	4.03
D 0.2, T 0.6	SS Total Daily PAR	70.08	70.09	68.90	68.08
	Total Annual PAR	7438	7332	7116	6293
	RMSD	3.13	5.09	6.13	3.60
D 0.3, T 0.6	SS Total Daily PAR	69.67	70.17	69.04	67.98
	Total Annual PAR	7461	7426	7225	6470
	RMSD	2.79	4.66	5.61	2.72
D 0.3, T 0.7	SS Total Daily PAR	68.61	70.35	69.56	68.51
	Total Annual PAR	7749	7857	7667	6826
	RMSD	2.03	2.67	3.58	1.61

Data collected using a network of HOBO sensors were used to ground-truth the accuracy of the T-SPAR model. Calibration measurements in the field revealed sensor malfunction due to low temperatures. Sensors reliably responded to overall changes in total surface PAR, but the magnitude of their response was unpredictable. All sensors were prone to under- and over-responding. This made it impossible to use point field measurement to estimate the accuracy of DEM surface predictions. Network measurements were instead used to determine the topographic model's ability to predict changes in surface PAR on spatial and temporal scales.

The network of sensors was deployed in each basin for over a week at a time. A period of three consecutive days with clear atmospheric conditions was chosen from each sample run,

corresponding to 10/25 through 10/27/2015 for the Lake Fryxell basin, 11/9 through 11/11/2015 for the Lake Hoare basin and 11/27 through 11/29/2015 for the Lake Bonney basin. Daily met station and handheld PAR measurements for these intervals had similar diurnal envelopes and consistent daily maximums and minimums. Observed and estimated values were plotted together for comparison (Fig. 11).

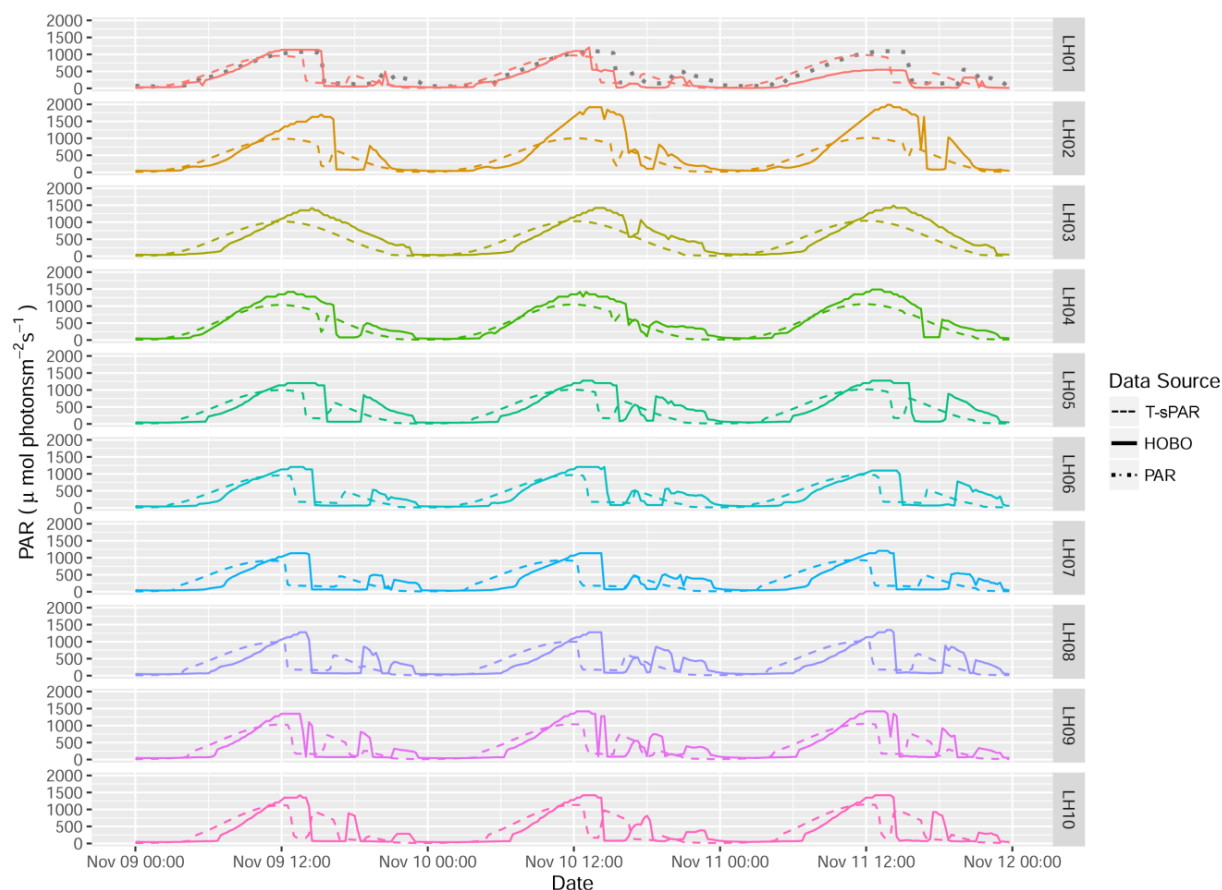


Fig. 11. Surface PAR measured with HOBO pendant light sensors plotted against Point T-sPAR estimates.

Modeled results show a good fit in terms of predicting large topographic shading events. Data for the Lake Hoare basin illustrate this correlation most clearly (Fig. 11). Several of the modeled sensor locations show a gradual reduction of the trough created by topographic shading as the solar elevation increases from day to day. The main difference between estimated and

observed values is their temporal synchronization. Modeled values have a tendency toward “occurring” before the actual observation. This is an artifact of the spatial resolution of the DEM combined with the sky view resolution and ArcMap’s Sun position algorithm. At a resolution of 30 m, shadows will be estimated to be present over areas both before and after they are physically present. A small error in the Sun position algorithm will predict a location that is off by a few degrees, which will have an impact on modeled ray tracing within the DEM. Similarly, a coarse resolution for the sky view will affect the Sun position and subsequent ray tracing.

4.5. Area T-sPAR

The parameters for the best fit Point T-sPAR model (D 0.3, T 0.7) were used to estimate surface PAR for all of Taylor Valley for the entire austral summer (Fig. 12). “Solargraphic” contour intervals were drawn for the surface PAR map to facilitate the interpretation of values. As expected, areas of high elevation and north facing slopes receive the greatest amounts of surface PAR while south facing slopes received the least total radiation. Values above 10 000 annual mol photons m^{-2} are only found at the highest points along the ridgeline, where a high SVF allows for unobstructed incident radiation throughout the entire day and at the lowest solar angles. The south facing slopes of the Asgard Range generally receive 4000 to 6000 annual mol photons m^{-2} , with the western ends of the Lake Bonney and Lake Hoare basins affected the most. The north facing slopes of the Kukri Hills generally receive 8000 to 10 000 annual mol photons m^{-2} , and surface area values increase from east to west. PAR values on the valley floor range between 6000 and 8000 annual mol photons m^{-2} , with the lowest parts of the valley receiving less PAR than higher ground.

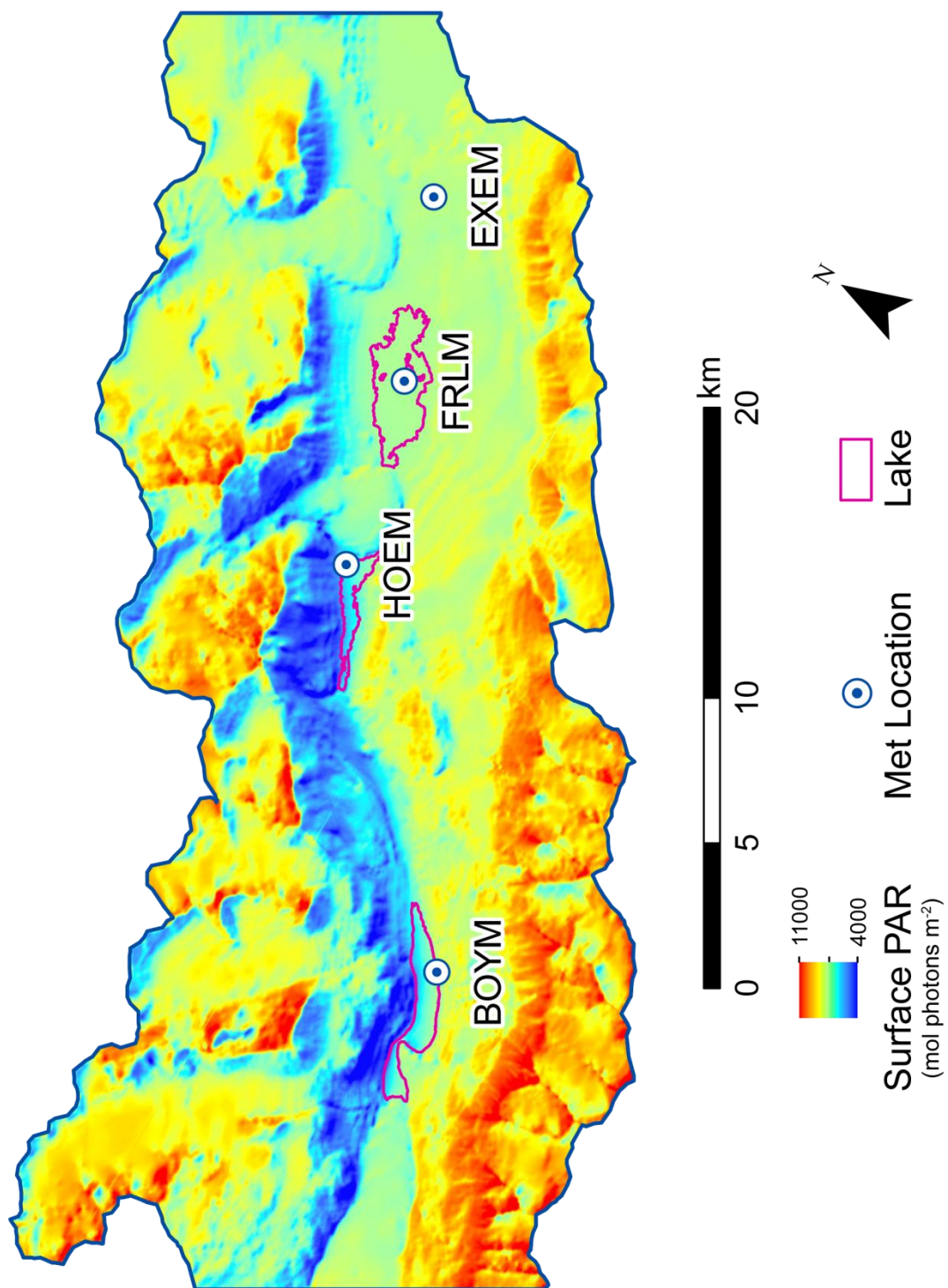


Fig. 12. Total annual surface PAR map for the Taylor Valley basin estimated using the Area T-sPAR model.

The effects of annual topographic shading on each lake are evident in Taylor Valley's individual lake maps (Fig. 13). Lake Fryxell, which occupies the widest basin and is surrounded by the lowest ridgeline compared to the other lakes, is the only lake to receive between 7000 and 8000 annual mol photons m^{-2} across its entire surface, and overall annual surface PAR generally increases from west to east. Lake Bonney and Lake Hoare both abut the southern slopes of the Asgard Range. As a result, topographic shading bisects the distribution of surface PAR for these two lakes between northern and southern shores. Annual surface PAR on Lake Bonney is roughly evenly split with the northern edge of the lake receiving 6000 and 7000 annual mol photons m^{-2} , while the southern edge receives 7000 and 8000 annual mol photons m^{-2} . Most of Lake Hoare's surface receives 6000 and 7000 annual mol photons m^{-2} due to topographic shading from the west. Only the lake's easternmost edge receives 7000 and 8000 annual mol photons m^{-2} (Fig. 13). Area T-sPAR maps can also be used to calculate summary statistics such as total PAR across any surface of interest like an entire valley basin or a lake, and normalized by total surface area to allow for comparison (Table VII).

A

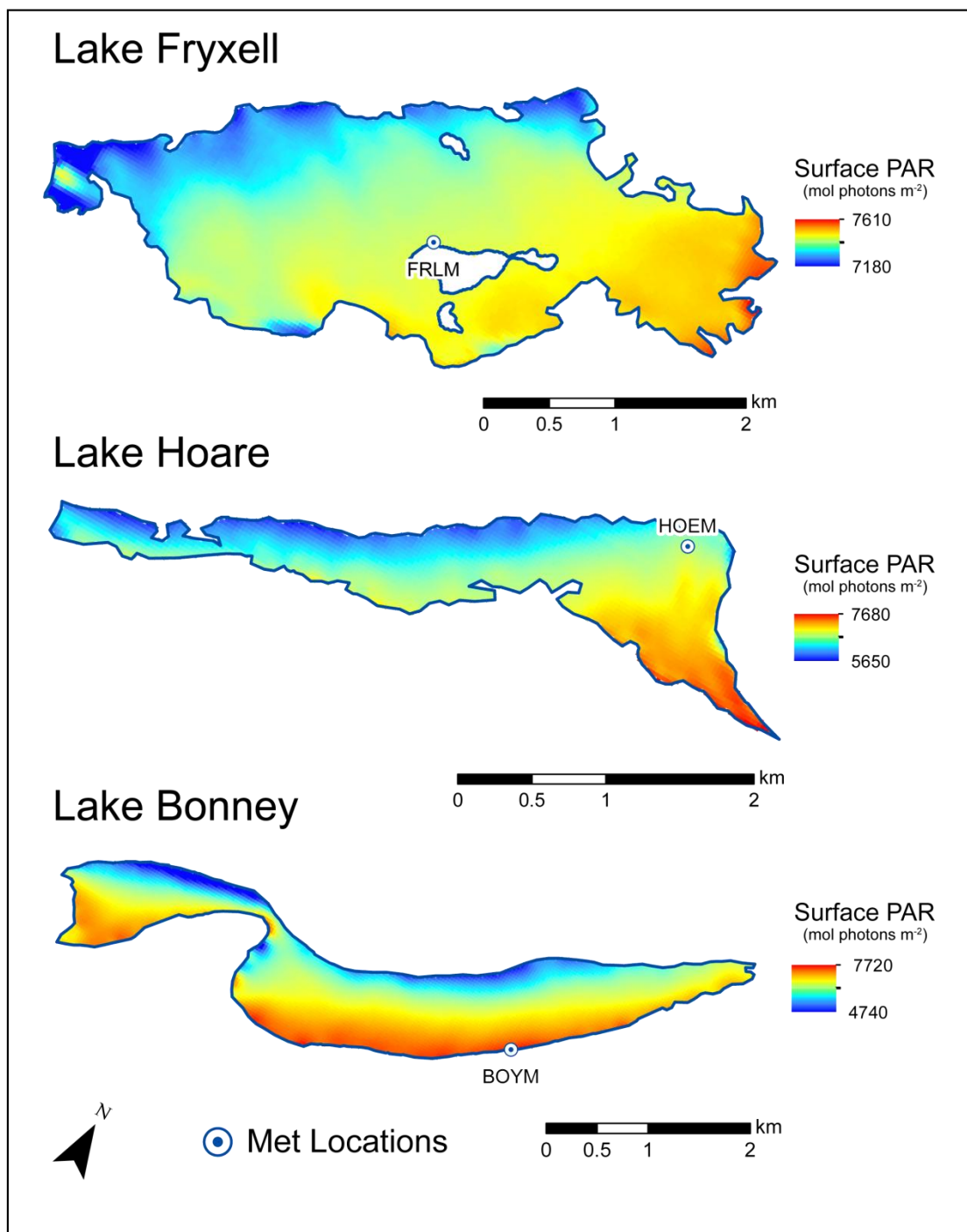


Fig. 13. Total annual surface PAR by lake surface estimated using the Area T-sPAR model. A. Surface PAR lake maps with scale set to range of values by individual lake surface. Lakeshore boundaries set to 12/19/2014. Lake maps use different distance scales.

B

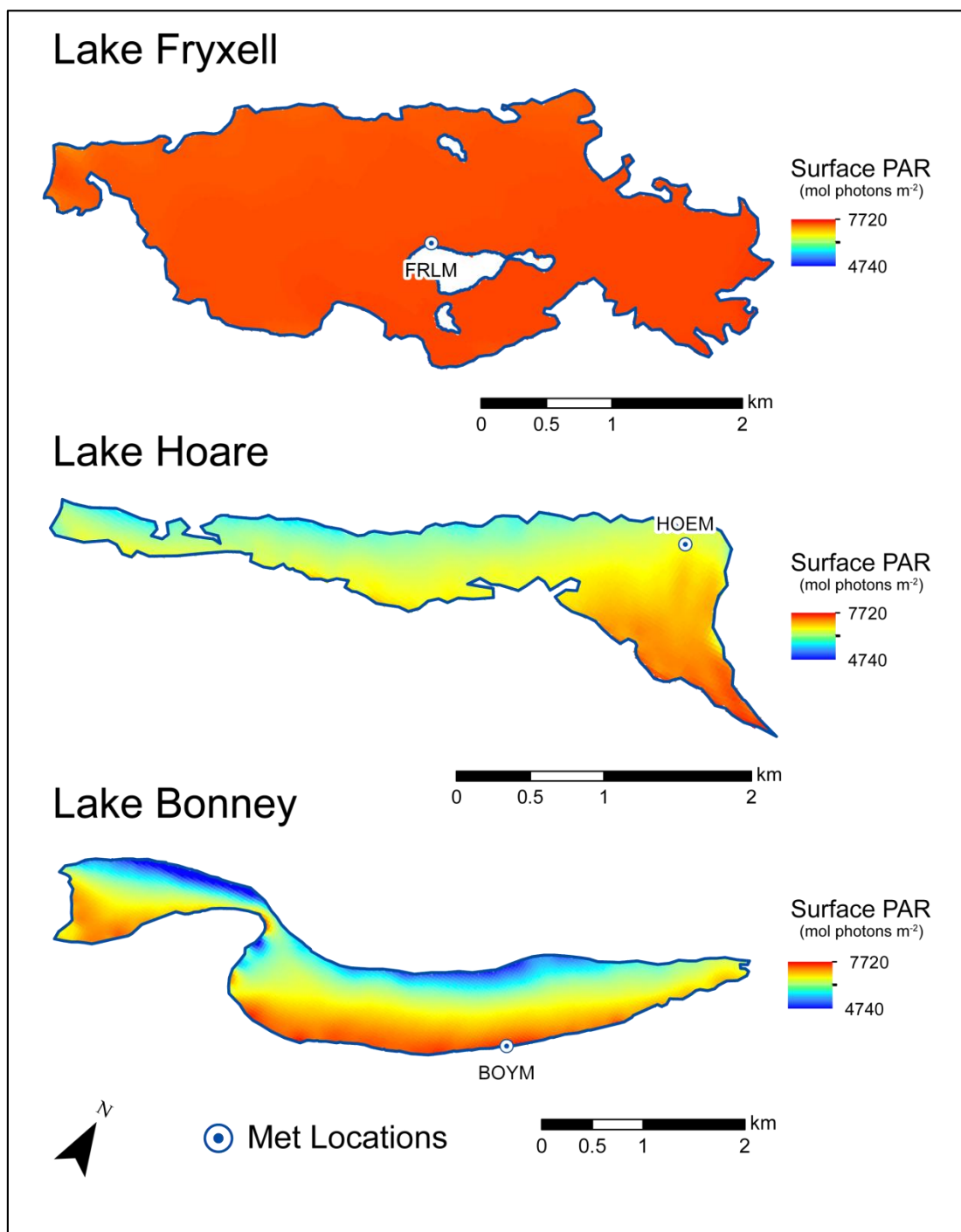


Fig. 13. (continued) B. Surface PAR lake maps with scale set to common range of values shared by all lake surfaces. Lakeshore boundaries set to 12/19/2014. Lake maps use different distance scales.

Table VII. Summary statistics for total annual surface PAR estimated by Area T-sPAR.

Area	Range (mol photons m ⁻²)	Total PAR across surface (giga mol photons)	Total PAR by surface area (mol photons m ⁻²)
Taylor Valley	3525 – 11255	5327.02	7920
Lake Fryxell	7185 – 7609	51.81	7596
Lake Hoare	5647 – 7679	15.32	6750
Lake Bonney	4741 – 7724	31.28	6903

Additional surface PAR distribution maps were developed on bi-monthly intervals for Taylor Valley using the Area T-sPAR model (Fig. 14). The model aggregates total daily surface PAR over the specified time interval, and reports the daily average by dividing over the number of days in the interval (14 days for most maps, with the exception of the summer solstice map, which includes 15 days). These maps help visualize the progressive changes in surface PAR over the course of the austral summer and can be used by field parties to identify future sampling sites. The shorter timescales of these surface PAR estimates can also be correlated with indexes of primary productivity and measurements of underwater PAR

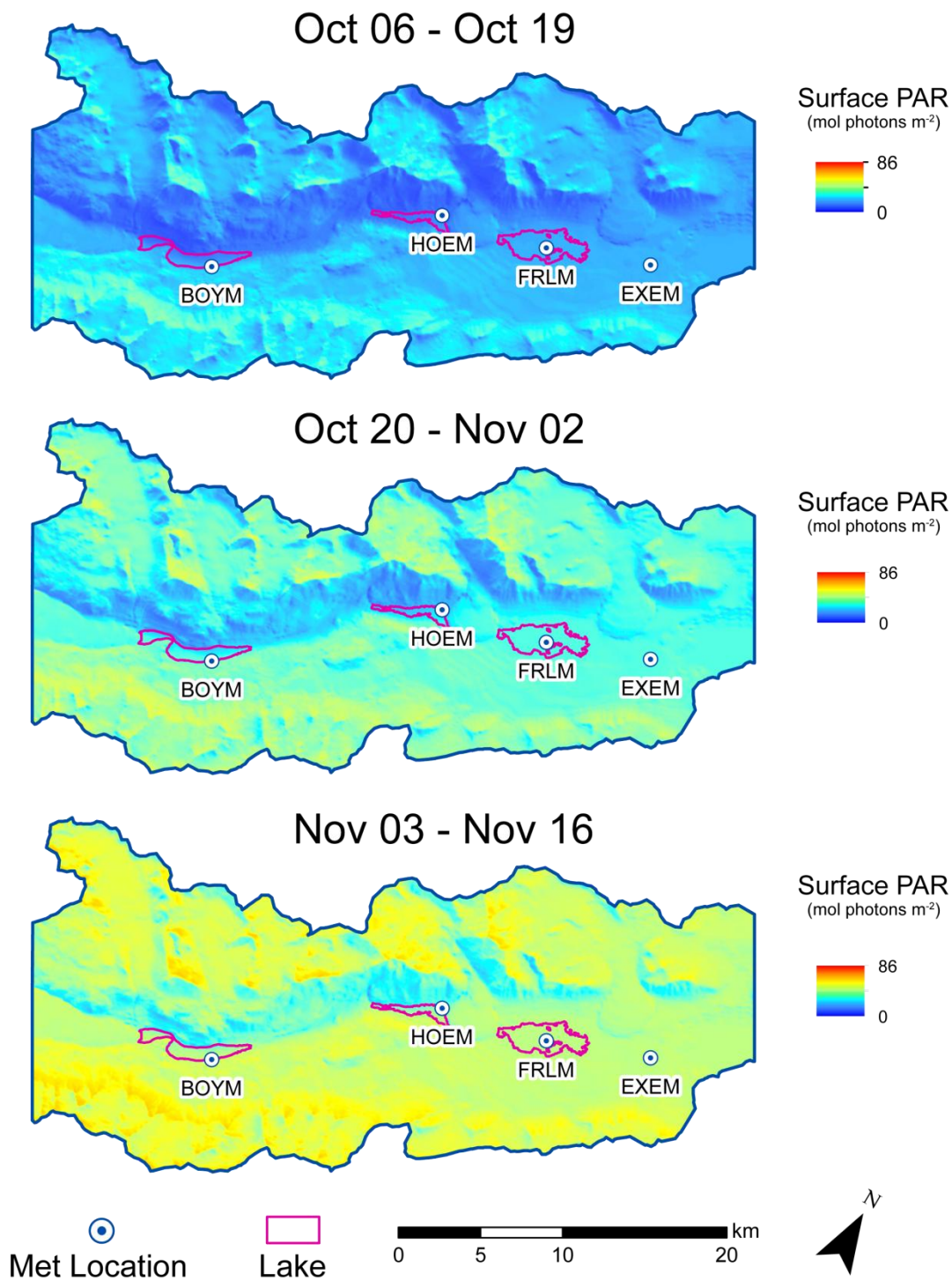


Fig. 14. Bi-monthly surface PAR distribution maps covering a six week period between Oct 6th and Nov 16th. Reported surface values correspond to the daily average over the timespan ending at 23:59:59 of the listed date. Maps use the same distance scale. The surface PAR scale is set to the range of values observed over the entire austral summer.

4.6. T-sPAR Toolbox

The T-sPAR Toolbox includes ArcMap models that automate the process of creating new Point and Area surface PAR estimates. The models use the parameters described in this study as defaults to calculate surface PAR values in the Taylor Valley basin. They apply the necessary scaling coefficients via raster math to generate daily totals of surface PAR. The main user-defined input is the date or desired timeframe to provide estimates for. The cloud cover factor calculated from the CC model scales results to constrain estimates by meteorological observations.

The Point T-sPAR Toolbox model requires the latitude and longitude coordinates for the point or points of interest in decimal degrees. Values are input using a simple comma space value (CSV) template table to project the points onto the DEM. The model is set to provide estimates for clear conditions by default, but can be modified by the user as desired. When results are constrained by atmospheric conditions, multipoint calculations should be limited to locations in close proximity to each other, ideally within the same lake basin. The Point T-sPAR model only accepts a single value for the CC factor and applies it uniformly to all points in the table. Coordinates in different lake basins should be calculated separately using the CC factor for the nearest met station. The model interprets each point's spatial relationship and calculates surface PAR for the coordinates, outputting the attribute table results to a file format that can be further manipulated outside of ArcMap.

The Area T-sPAR Toolbox model generates surface PAR raster maps for all of Taylor Valley and for each of the major lakes. This model requires the input of CC factors for all four meteorological stations. The spatial relationship of CC factors is interpolated across the entire

valley using inverse distance weighing (IDW) to create a cloud cover raster mask (Fig. 15 A). IDW interpolation creates a sphere of influence around each of the four sample points that decreases with distance when other sample points are present within the sphere. The result is a smooth gradient transition from point to point.

The Area T-sPAR Toolbox estimates total daily surface PAR based on *cloudless* conditions (Fig. 15 B). It then combines the estimate map with the cloud cover mask using raster multiplication to create a cloud cover corrected map (Fig. 15 C). Surface PAR pixel values in the final raster map are scaled down based on the magnitude of the CC values to a maximum of 50% of the pixel's *cloudless* potential. The cloud cover corrected map is clipped using the 12/19/2014 lakeshore boundaries to produce surface PAR maps for each individual lake. Finally, solargraphic contour lines with an interval of 1 mol photon m⁻² are drawn for each lake to help distinguish surface values.

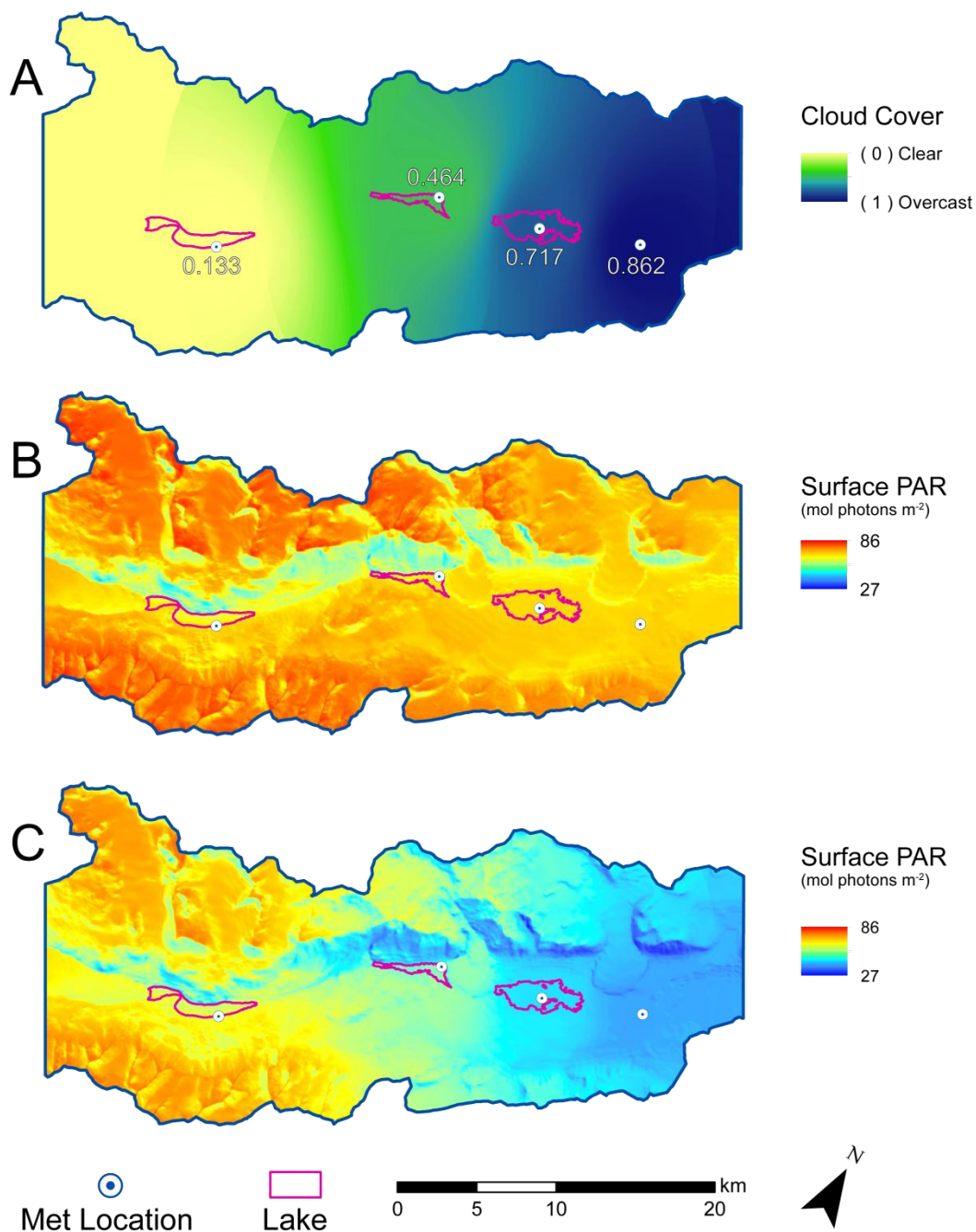


Fig. 15. Surface PAR map with an interpolated cloud cover correction for a hypothetical December 19th created with the Area T-sPAR Toolbox. A: Cloud cover raster mask shows interpolated atmospheric conditions based on input values for each met station. Overcast conditions dominate on the eastern end of the valley while clear conditions prevail in the west. B: Estimated surface PAR without cloud cover correction. Values range between 39 and 86 daily mol photons m^{-2} . C: Estimated surface PAR corrected with cloud cover mask. The new raster shows the impact of cloud cover on the eastern side of the valley with only a slight reduction on the western end. Values range between 27 and 80 daily mol photons m^{-2} .

5. CONCLUSIONS

Solar radiation is the major driver of climatological and biological processes on Earth. In the McMurdo Dry Valleys, PAR provides energy for the photoautotrophs in this extreme ecosystem. Developing an accurate model that can predict surface PAR is essential to understanding primary productivity in this unique ecosystem. Meteorological observations collected and maintained by the MCM LTER present a unique opportunity to advance understanding of the constraints on life in Taylor Valley's polar soils and ice-covered lakes.

Statistical analysis of records from BOYM, EXEM, HOEM and FRLM meteorological stations produced seasonal envelopes for instantaneous surface PAR and estimates for total annual surface PAR. These observation envelopes represent potential absolute maximums for *cloudless* conditions. These ideal empirical values are used to constrain a topographic model of surface PAR. Quantifying ideal conditions is necessary to overcome the need to model cloud cover, a ubiquitous and unpredictable constraint on the availability of surface PAR.

The meteorological record indicates that PAR starts increasing after the winter in Taylor Valley around August 9th and falls below detection on May 4th. Instantaneous maximum expected PAR under *cloudless* conditions recorded at the meteorological stations included in this study range from 1540 to 1620 μ mol photons $m^{-2} s^{-1}$ for the austral summer solstice. Total expected daily PAR for the solstice ranges from 65 to 73 daily mol photons m^{-2} and total annual PAR is calculated between 6940 to 8480 annual mol photons m^{-2} . Generally, daily and total surface PAR is greater in the eastern end of the Taylor Valley basin, while the largest daily instantaneous values of PAR are recorded at Lake Bonney. Lake Hoare receives the least PAR on a daily and annual basis and has the lowest instantaneous observations.

Comparison of expected and measured total daily PAR was used to determine local cloud cover. Examination of records for witnessed overcast days and snow events during the 2014/2015 and 2015/2016 field seasons suggest such conditions cause an $\approx 50\%$ decrease in total daily PAR. This ratio was used to bin measured daily totals into four categories: clear, scattered, broken and overcast. The CC model shows EXEM met has the highest frequency of overcast days while BOYM has the lowest, suggesting a positive correlation between proximity to the coast and total days with high cloud cover. The CC model also shows that BOYM, EXEM and FRLM met stations observe increasingly overcast conditions toward the end of the austral summer, peaking during the month of February. HOEM met on the other hand records highest frequency of over cast conditions during the month of December.

Diffuse and reflected radiation accounts for 15 to 26% of global radiation, which is consistent with fractions reported at other latitudes. Global surface PAR appears to attenuate to the background diffuse fraction at a distance of ≈ 35 m from the edge of the umbral horizon.

ArcMap's point and solar radiation tools are convenient methods for predicting surface PAR in the McMurdo Dry Valleys where spatial and temporal constraints limit extensive empirical measurements. Topographic radiation modeling has been shown to be effective at predicting surface radiation at mid latitudes. A number of combinations of atmospheric diffuse fraction and transmittivity were tested to find the best fit model for meteorological observations. Values of $D = 0.3$ and $T = 0.7$ had the lowest root mean standard deviation (between 1.6 and 3.6 daily mol photons m^{-2}) of all models tested. Using these parameters, the Point T-sPAR model predicts EXEM met to have the highest total daily PAR around the summer solstice in agreement with meteorological observations. Point T-sPAR fails to predict FRLM met as the location with the second highest amount of total daily PAR favoring BOYM met instead. The cause for this

discrepancy likely lies in the low solar angles that characterize radiation in the McMurdo Dry Valleys. ArcMap is not capable of resolving radiation values at the lowest solar angles, and characteristically under-predicts the radiation envelope during the weeks leading up to and following the summer solstice. Further research into using topographic radiation models at high latitudes would greatly improve this model.

The T-sPAR model's spatial and temporal accuracy were tested using a network of sensors deployed across each basin. Comparison of estimated point values against observations shows a slight offset favoring premature predictions of increased surface PAR and topographic shading. These errors are likely artifacts of the models spatial resolution. Using a DEM with a pixel resolution greater than 30 m may improve accuracy at the cost of computation speed. Increasing the sky view resolution may also improve this accuracy. The observed offset has little consequence for estimates on daily timescales and is ignored for the purposes of this study.

Point T-sPAR estimates were used as guidelines to estimate annual surface PAR for Taylor Valley as a whole (D 0.3, T 0.7). The Area T-sPAR model yields normalized values for the entire basin of 7920 annual mol photons, estimating 7596 annual mol photons across Lake Fryxell's surface, 6903 annual mol photons for Lake Bonney's, and 6750 annual mol photons for Lake Hoare. Additionally, bi-monthly surface PAR maps identify total aggregate values on timescales that can be used in the field to inform the choice of future sampling sites, and constrain net primary productivity of Taylor Valley's ice-covered lakes.

The T-sPAR Toolbox applies the results of this study and incorporates them into a user friendly package that estimates point and area surface PAR. Minimal user input and a simple graphic interface facilitate the estimations using meteorological data for any day of the Antarctic austral summer. The Point T-sPAR Toolbox model allows users to calculate single point

approximations and correct estimated *cloudless* surface values with modeled cloud cover observations. The Area T-sPAR Toolbox interpolates cloud cover across Taylor Valley based on calculated CC factors for each met station creating a raster mask that corrects whole area surface PAR estimates based from topography. Together, the T-sPAR models improve the overall understanding of PAR in one of Antarctica's most unique ecosystems and help constrain primary productivity within Taylor Valley's ice covered lakes.

APPENDICES

APPENDIX A

T-sPAR Toolbox Instruction Manual

The T-sPAR Toolbox is a collection of ArcGIS models developed in ArcMap that facilitate the estimation of surface PAR in Taylor Valley, Antarctica. The toolbox is nested inside the TV_T_sPAR File Geodatabase along with all essential feature classes and raster datasets required for processing (Fig. 1, Appendix A). The toolbox includes 3 models listed alphabetically.

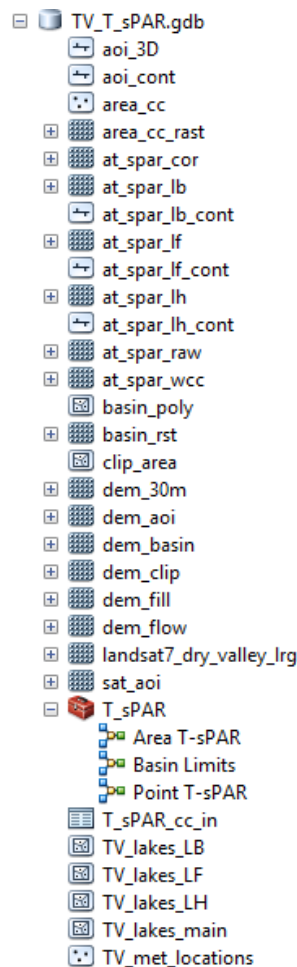


Fig. 1, Appendix A. Catalog tree of the TV_T_sPAR File Geodatabase. Models to estimate surface PAR are found inside the T_sPAR Toolbox.

Basin Limits

The Basin Limits model is used to reduce the file size of the DEM available from the MCM LTER Data repository (<http://mcm.lternet.edu/power-search/data-set>). This model should be run first, before using either the Point T-sPAR or Area T-sPAR model when working with a new basin. The output of this model for the Taylor Valley basin has been saved in the TV_T_sPAR File Geodatabase and does not need to be rerun if the “clip_area” feature class is unchanged.

To run the Basin Limits model, double click the file name. This opens the model’s graphic user interface (GUI) (Fig. 2, Appendix A). The model is set to calculate the Taylor Valley basin by default. The model requires a DEM, a Satellite overlay image, the desired contour interval in meters, the clip area and the output directory. Details about the tool and each parameter can be toggled on or off with the “Show Help >> / << Hide Help” button.

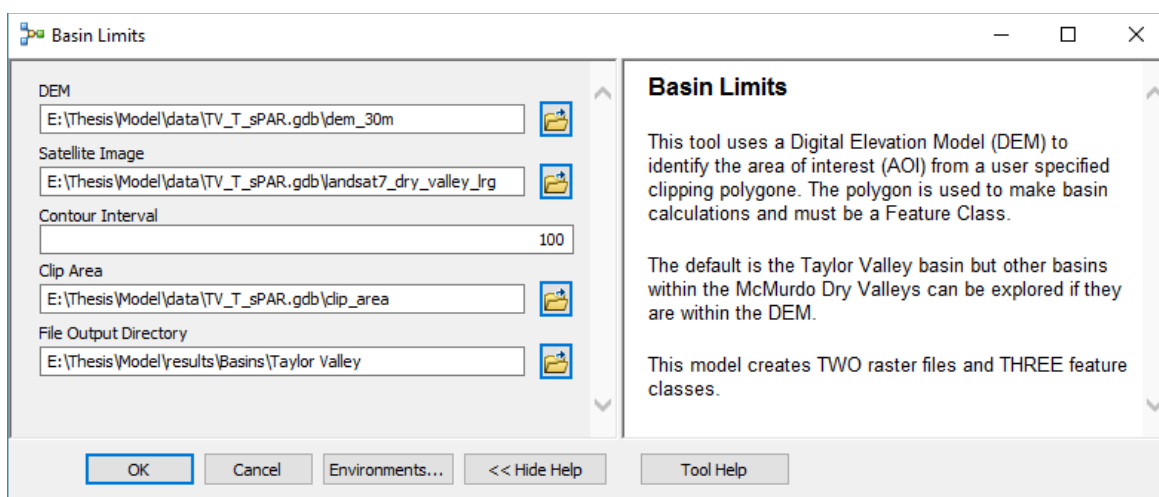


Fig. 2, Appendix A. Graphic User Interface for the Basin Limits model with default parameters. The model has 5 user inputs to establish the area of interest.

APPENDIX A (continued)

Output of this model includes five main files: two raster images and three feature classes / shapefiles. The “dem_aoi” raster is the most important output file. It is the clipped area corresponding to the basin of interest within the DEM. The “sat_aoi” file is the Satellite image clipped to match the DEM basin of interest. The “basin_poly” feature class defines the limits of the area of interest. The “aoi_cont” feature class includes vectors of the specified contour interval derived from the DEM. The “aoi_3D” feature class calculates “Z” values from contour intervals to create 3D features that can be further examined in ArcScene or used to create triangulated irregular networks (TIN).

To view the inner functionality of the Basin Limits model and modify hard coded parameters right click on the file name and select “Edit.” This opens the model editor and the model flow chart (Fig. 3, Appendix A). It is recommended to copy the model before making any major modifications as these are permanent.

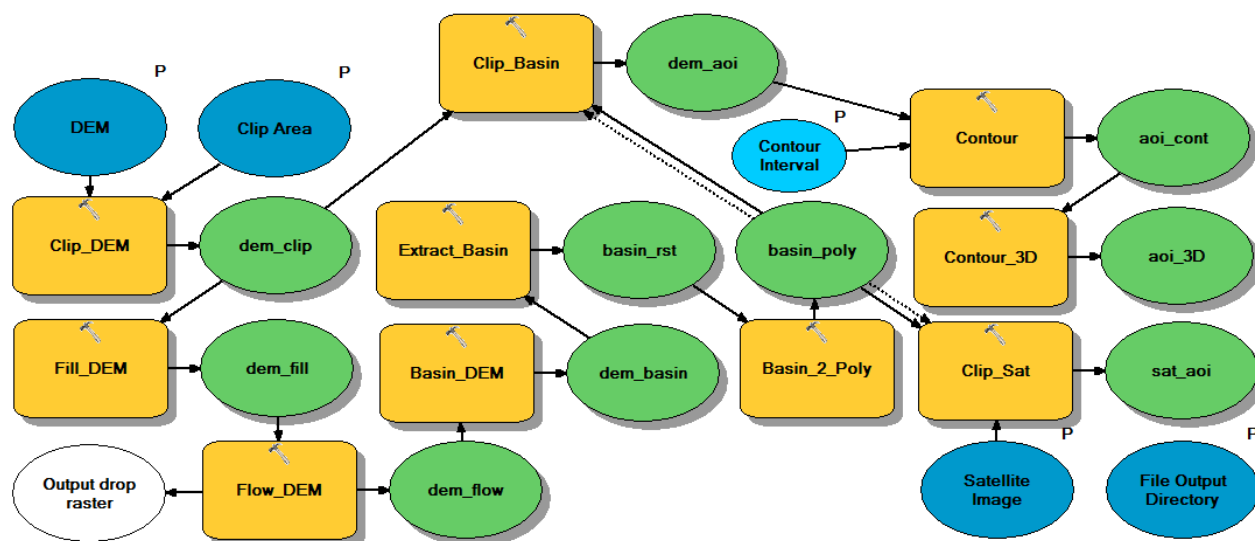


Fig. 3, Appendix A. Basin Limits model flow chart viewed in the ArcGIS model editor. Inputs are in blue, processes in yellow, outputs in green. Dotted lines indicate precondition fields. The letter “P” indicates fields that can be manipulated by the user.

APPENDIX A (continued)

The “Extract_Basin” process is known to cause errors in the model if the clip area feature class is changed. This is due to a known error with ArcGIS’s SQL that prevents selecting a maximum as a variable causing the model to encounter a fatal error if the hard coded maximum value is not found. To fix this problem, open the attribute table for the “dem_basin” raster, sort the list by “Count” and identify the new maximum value. Double click the *Extract_Basin* process to replace the existing value of “747483” for the new value in the SQL “Where clause” field (Fig. 4, Appendix A).

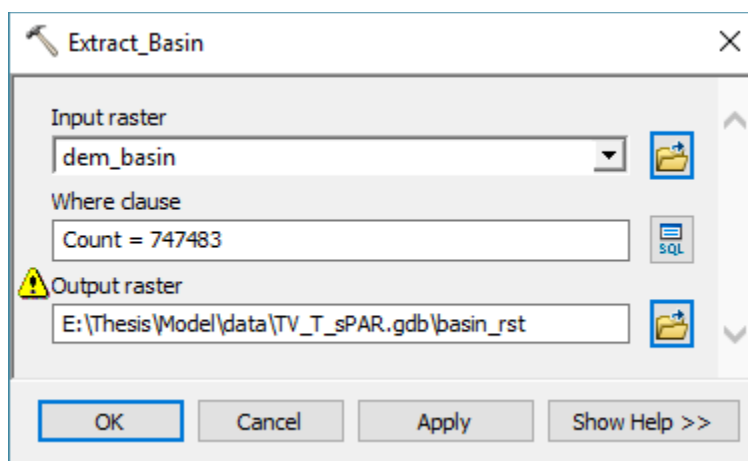


Fig. 4, Appendix A. Extract Basin process parameters from the Basin Limits model. The hard coded “Count = 747483” causes errors when the clip area is changed and should be replaced by the new maximum “Count” for the “dem_basin” raster.

Point T-sPAR

The Point T-sPAR model is used to estimate point surface PAR values calculated using the “dem_aoi” raster. This model can be run either before or after the Area T-sPAR model and works for any point within the area of interest. The model has a similar GUI with the same feature functionality as the Basin Limits model (Fig. 5, Appendix A). The time configuration for the Point T-sPAR model should always be kept to “Within a day.” Use of other time

APPENDIX A (continued)

configurations can cause estimate errors. The user can enter the Julian day to be estimated, or look up the desired calendar day by clicking on the calendar icon. The default is to estimate a full 24 hours, but shorter timeframes may be chosen. Output values are in $\text{mol photons m}^{-2} \text{ h}^{-1}$, which are automatically aggregated to the interval sum for “cloudless” atmospheric conditions.

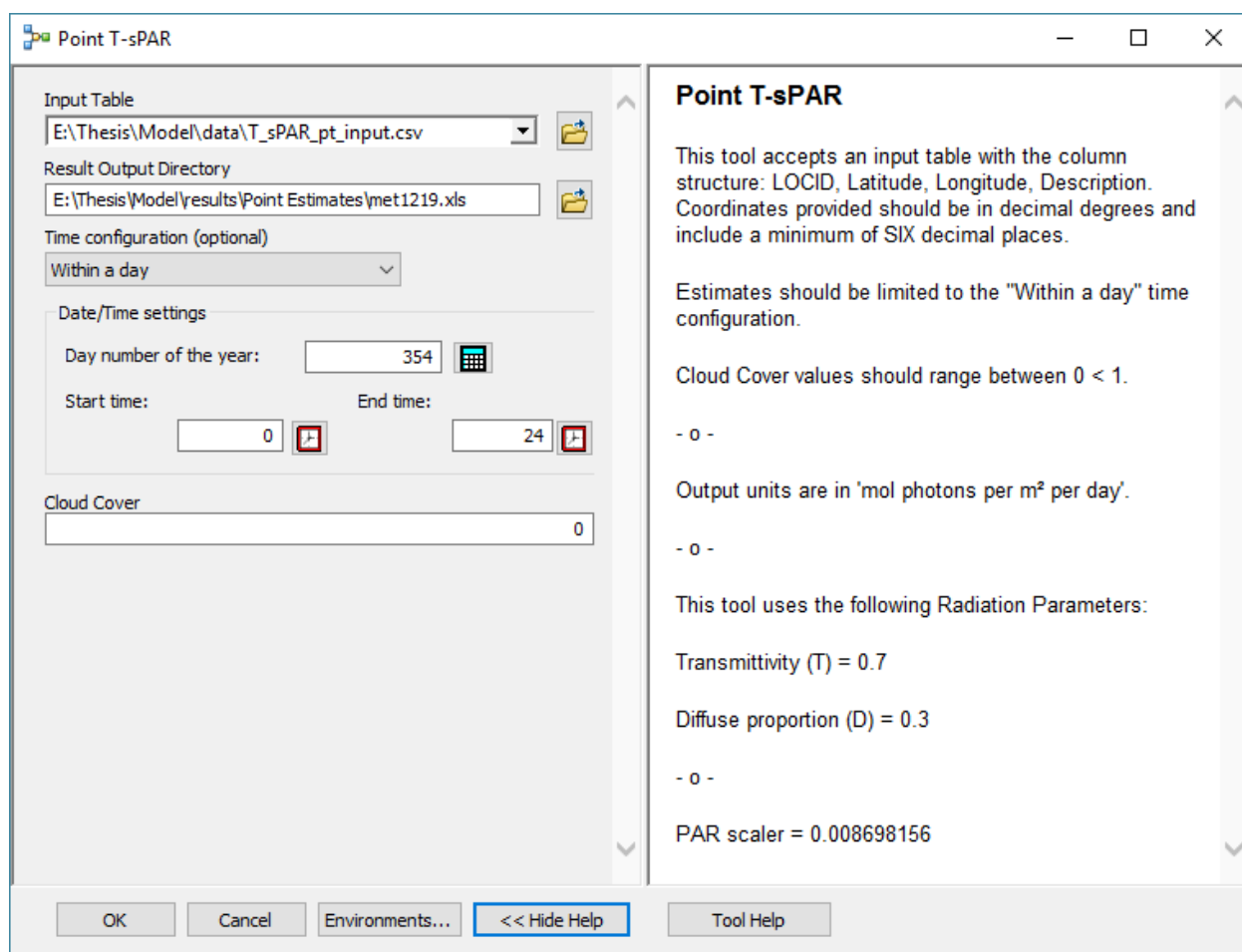


Fig. 5, Appendix A. Graphic User Interface for the Point T-sPAR model with default parameters. The model has 4 user inputs required to generate estimates.

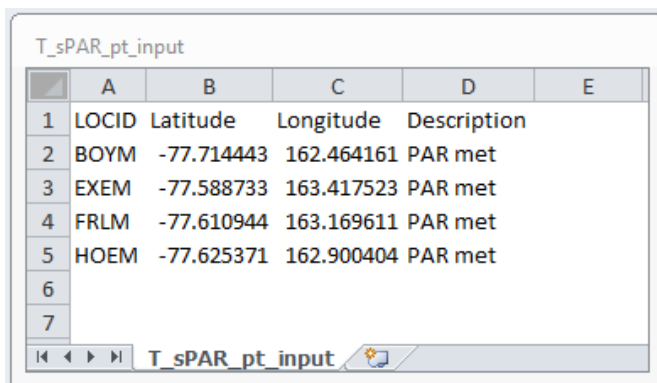
The Cloud Cover value is a number between $0 < 1$ that represents observed cloud cover where zero is equal to clear atmospheric conditions and one is equal to completely overcast. This value is calculated from met station observations using the CC model. This value acts as a scaler that decreases the surface PAR value estimated for *cloudless* conditions and applies it uniformly

APPENDIX A (continued)

to all values within the input table. For best results, Point T-sPAR calculations should use the CC factor for the met station closest to points of interest and points should be limited to a single lake basin area. Points distributed across multiple lake basins should be calculated separately with the appropriate CC value.

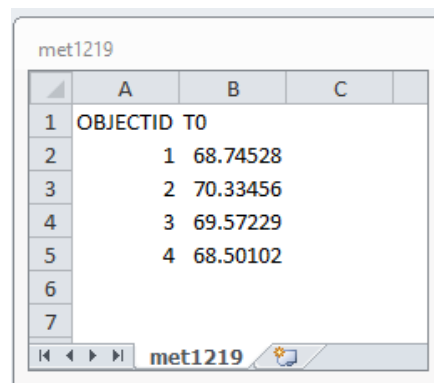
The Point T-sPAR model's main input and output are tables of values. The model requires an input table with coordinates in decimal degrees with a minimum of six decimal places for proper accuracy (Fig. 6 A, Appendix A). The table should be saved as a MS-DOS CSV file to avoid any issues with file compatibility. Since the output of this model is a single file, the user must define both a file name and the directory where to output to. Output files provide a single value for the total surface PAR at each point estimated over the specified time period and are reported in the same order as they were input (Fig. 6 B, Appendix A).

A



	A	B	C	D	E
1	LOCID	Latitude	Longitude	Description	
2	BOYM	-77.714443	162.464161	PAR met	
3	EXEM	-77.588733	163.417523	PAR met	
4	FRLM	-77.610944	163.169611	PAR met	
5	HOEM	-77.625371	162.900404	PAR met	
6					
7					

B



	A	B	C
1	OBJECTID	TO	
2	1	68.74528	
3	2	70.33456	
4	3	69.57229	
5	4	68.50102	
6			
7			

Fig. 6, Appendix A. Sample Point T-sPAR input and output tables. A. Input Table column headers must match this example and the coordinates for points to be estimated should be given in decimal degrees with at least six decimal places. B. Output table does not retain location IDs but records are kept in the same order as they were input.

The T-sPAR model does accurately predict surface PAR for the summer solstice using the “Within a day” time configuration. To get accurate results it is necessary to use the “Special

APPENDIX A (continued)

days” time configuration. Changing the time configuration, however, causes additional errors due to certain parameters that are hard coded into the model. If it is necessary to run estimates for a time configurations other than “Within a day” a few parameters must be adjusted within the model editor. The “PAR conversion” process is known to cause errors if a different time configuration is used (Fig. 7, Appendix A). This process applies a series of calculations to the specified field “T0”. The “Special days” time configuration outputs summer solstice values to the “T2” field. In this case the simplest solution is to change the “Field Name” from T0 to T2 (Fig. 8, Appendix A) and substitute accordingly within the “Expression” parameter. If multiple fields need to be calculated, another alternative is to bypass the conversion process altogether and apply operations manually to the file output.

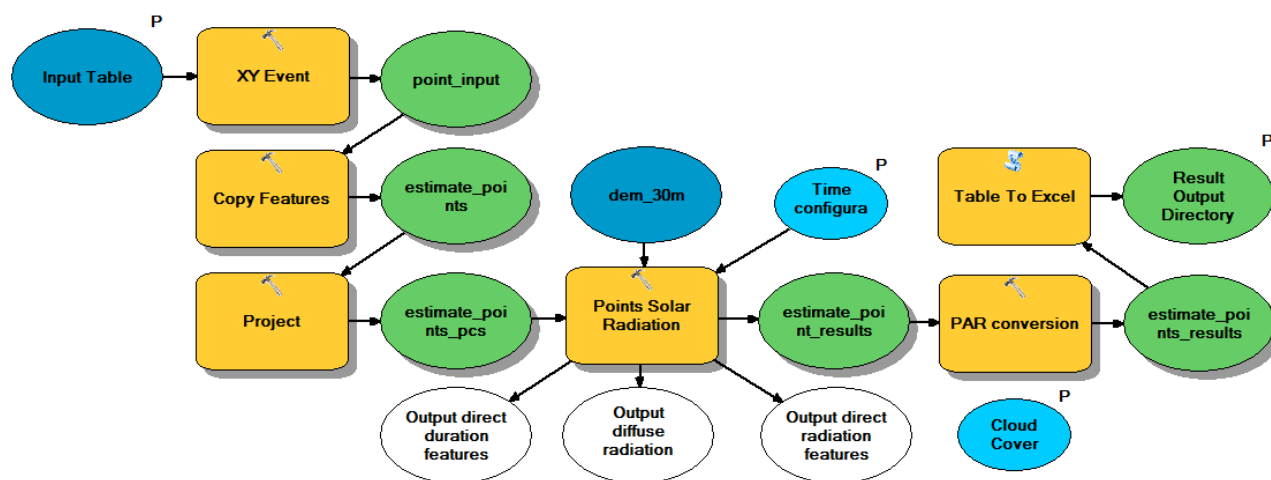


Fig. 7, Appendix A. Point T-sPAR model flow chart viewed in the ArcGIS model editor. Inputs are in blue, processes in yellow, outputs in green. The letter “P” indicates fields that can be manipulated by the user.

APPENDIX A (continued)

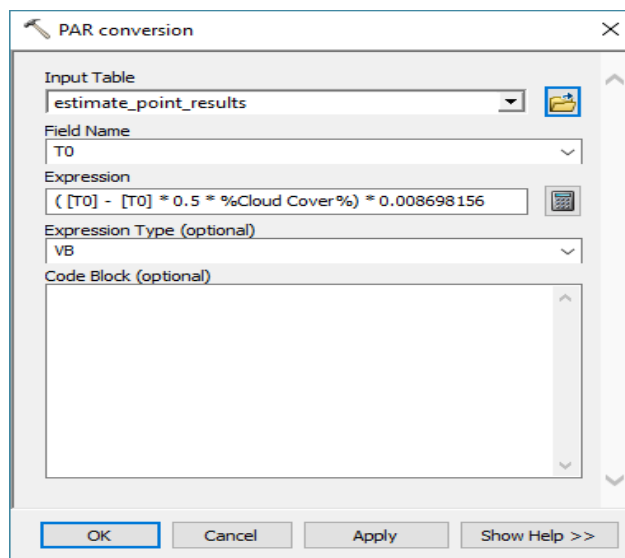


Fig. 8, Appendix A. PAR conversion process parameters from the Point T-sPAR model. This process corrects cloudless point estimates and multiplies values in “T0” by the PAR conversion factor of 0.008698156.

Area T-sPAR

The Area T-sPAR model generates maps of surface PAR distribution calculated using the “dem_aoi” raster. This model can be run either before or after the Point T-sPAR model. The model’s GUI is nearly identical to the Point T-sPAR model and shares the same feature functionalities and limitations (Fig. 9, Appendix A). The main difference from an input standpoint is that Cloud Cover values are input using a table instead of the GUI. This is because values need to be mapped by the model in order to spatially interpolate the effect of cloud cover across the entire valley area. The structure of the table itself is very similar to the one used for point value inputs, and should include CC factor values between $0 < 1$ with at least three decimal places (Fig. 10, Appendix A).

APPENDIX A (continued)

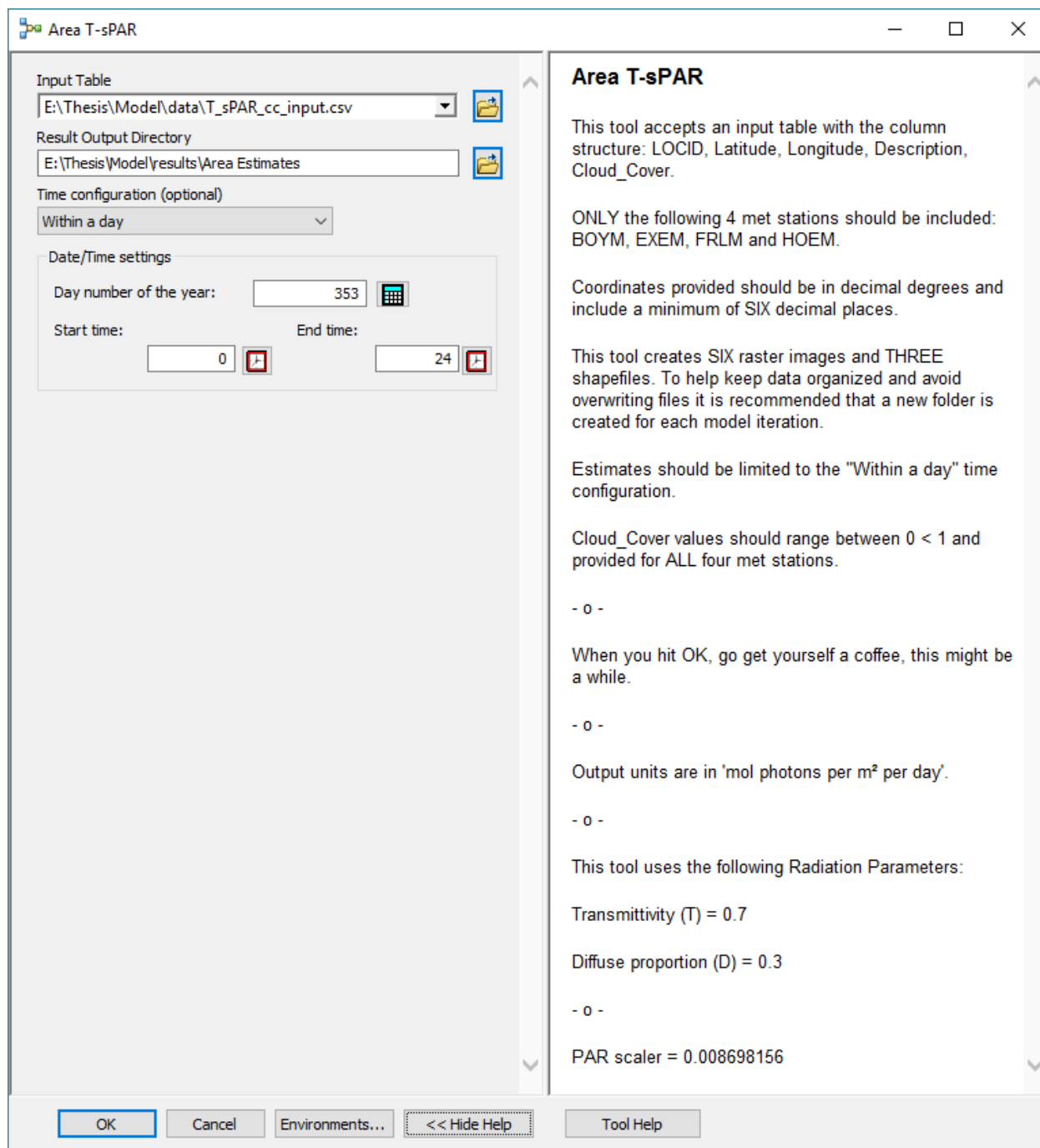
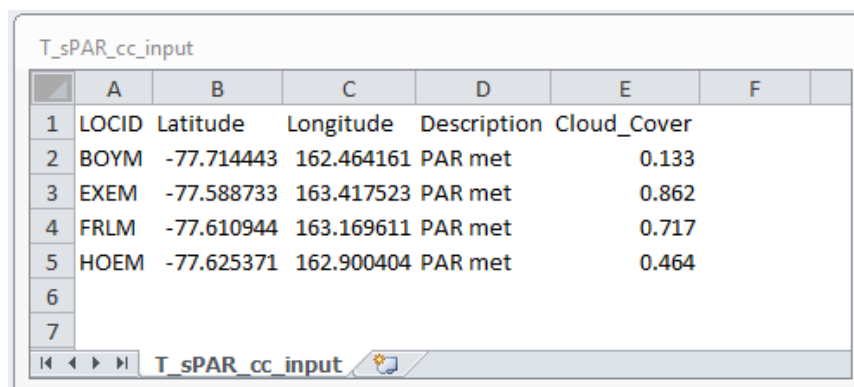


Fig. 9, Appendix A. Graphic User Interface for the Area T-sPAR model with default parameters. The model has 3 user inputs required to generate estimates. Cloud Cover values are input via a table.

APPENDIX A (continued)



	A	B	C	D	E	F
1	LOCID	Latitude	Longitude	Description	Cloud_Cover	
2	BOYM	-77.714443	162.464161	PAR met	0.133	
3	EXEM	-77.588733	163.417523	PAR met	0.862	
4	FRLM	-77.610944	163.169611	PAR met	0.717	
5	HOEM	-77.625371	162.900404	PAR met	0.464	
6						
7						

Fig. 10, Appendix A. Sample Area T-sPAR input table. Table column headers must match this example, coordinates for met stations should be given in decimal degrees with at least six decimal places and cloud cover values should range between $0 < 1$ with at least three decimal places.

The Area T-sPAR model generates six raster images and three feature class/shapefiles per iteration. It is recommended that a separate folder is used for every new run to keep files organized and prevent overwriting outputs. The “area_cc_rast” is the first raster generated by the model, and represents the cloud cover interpolated surface that is used to correct estimates. The “at_spar_cor” raster is the map of estimated surface PAR under *cloudless* conditions. The two raster files are combined using raster multiplication to create the third raster “at_spar_wcc”, which scales surface PAR values down based on the magnitude of observed cloud coverage. This raster is clipped by lake to produce three additional raster: “at_spar_lb”, “at_spar_lf”, and “at_spar_lh”. Finally, each lake raster is used to create solargraphic contour intervals with a unit value of 1 daily mol photon m^{-2} (Fig. 11, Appendix A).

APPENDIX A (continued)



Fig. 11, Appendix A. Area T-sPAR model flow chart viewed in the ArcGIS model editor. Inputs are in blue, processes in yellow, outputs in green. Dotted lines indicate precondition fields. The letter “P” indicates fields that can be manipulated by the user.

APPENDIX B

Anomaly detection

The MetAnalyst R script was used to generate time series PAR and SWR facet plots for all meteorological observations from 1996 to 2016. These plots revealed several data anomalies that were removed from the data set before further analysis. The most pronounced errors identified corresponded to BOYM met. A PAR sensor malfunction during late in the 2006/2007 field season recorded abnormally high values of PAR. Historic values for early February suggest that daily observed maximums should read near $1000 \mu \text{ mol photons m}^{-2} \text{ s}^{-1}$. Instead recorded values approached $1750 \mu \text{ mol photons m}^{-2} \text{ s}^{-1}$ (Fig. 1, Appendix B). This anomaly persists into the following field season when station maintenance likely corrected the problem. The overall shape of the meteorological record indicates a possible error in a multiplier coefficient. The correct multiplier can be derived from the station's maximum best fit curve, however, in order to calculate accurately those values must first be removed from the record.

The second major anomaly identified was a SWR sensor malfunction that occurred in early 2009, likely following station maintenance. Data show a marked drop in the SWR measurements (Fig. 2, Appendix B). Records show a coincident drop in PAR values over a span of several days, however PAR values return to expected values shortly thereafter while SWR values remain steady at 250 W m^{-2} for the rest of the year, into the Antarctic night and the following field season. Lack of response to radiative forcing as indicated by the PAR signal further supports the need to remove these data from the record.

APPENDIX B (continued)

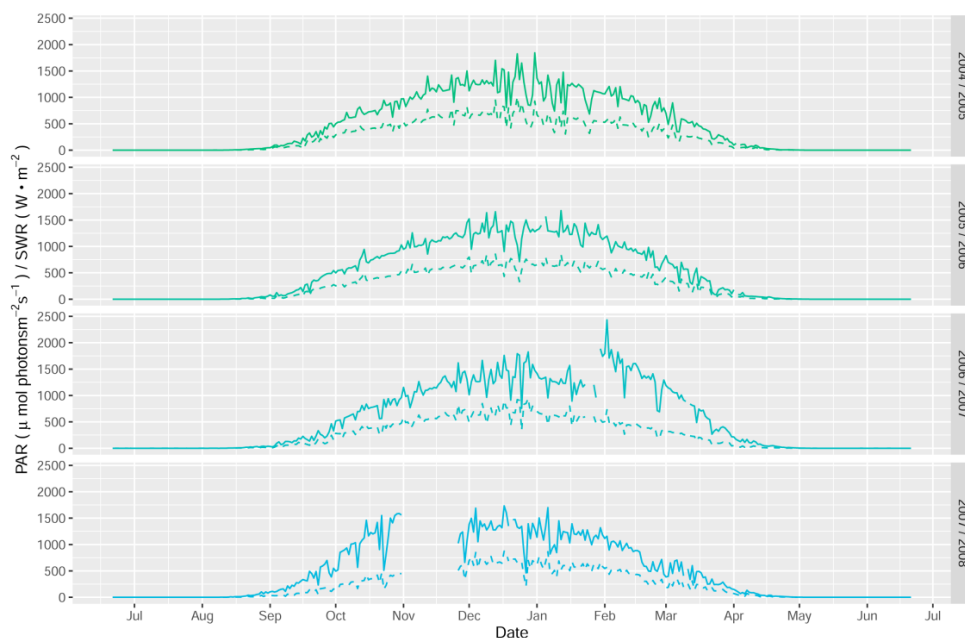


Fig. 1, Appendix B. Daily maximum observed values recorded at Lake Bonney over a 4 year period from 2004 to 2008. In February of 2007 an error with the PAR sensor caused abnormally high measurements.

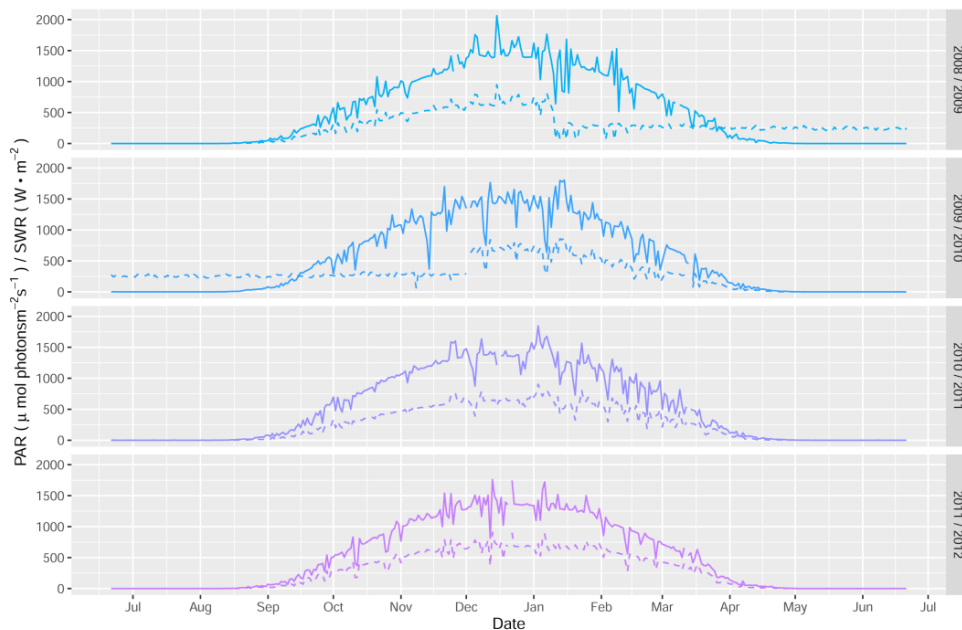


Fig. 2, Appendix B. Daily maximum observed values recorded at Lake Bonney over a 4 year period from 2008 to 2012. In January of 2009 an error with the SWR sensor caused measurements to flat line around 250 W m⁻² a value that persisted through the austral night and into the following summer.

APPENDIX B (continued)

One of the most interesting anomalies detected using the time series PAR and SWR facet plots was the discovery of a major snow event. The record shows both PAR and SWR measurements to that are one third of expected values for that time of year (Fig. 3, Appendix B). A drop of similar magnitude around the same period can be identified in the FRLM record; however that record returns to normal a few days later. A persistent weather system can be ruled out as the cause as it is unlikely that the signal would not be observed at other met stations. A permanent camera installed at Lake Hoare to monitor lake surface boulders revealed a thick blanket of snow across the lake supporting the notion of snow or ice obstructing the sensor. Analysis of these data by other means would likely have overlooked this anomaly given the agreement in between the PAR and SWR records. Visualizing the record this way is a quick and effective way of detecting data anomalies.

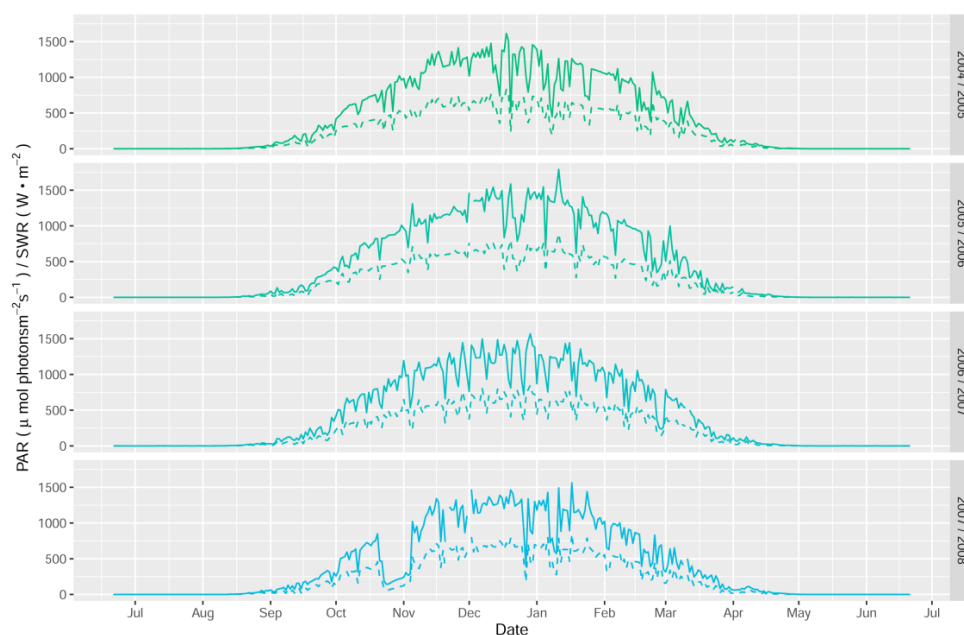


Fig. 3, Appendix B. Daily maximum observed values recorded at Lake Hoare over a 4 year period from 2004 to 2008. Both PAR and SWR radiation drop off dramatically for a two week period starting mid-October 2007. Photographs taken by a permanent camera at Lake Hoare that monitors boulder movement on the ice pan revealed a major snow event.

APPENDIX B (continued)

A different method of anomaly detection involves plotting PAR against SWR. The relationship between the two measurements is almost perfectly linear. Applying a linear regression to the values allows confidence intervals to be established that contain a percentage of the total data set. Values outside of the specified range can be categorically labeled to identify them for removal from the data set. This method is useful to identify anomalies that occur on shorter time spans ranging from a day to less than a week. The distribution of anomalies in the scatter plot provides some indication regarding the source of the anomaly. Single sensor under-response is much more likely than single sensor over-response. When SWR is plotted as a function of PAR, anomalous points that plot above the regression line likely originated from abnormally low PAR values with respect to SWR (Fig. 4, Appendix B). If the values plot below the regression line, the error is likely caused by an under-response of the SWR sensor. Sensor over-response cannot be completely ruled out until data is cross referenced against the time series.

An issue with this method is that variability in the record increases toward the height of summer. As a result, the confidence interval envelope enlarges, and it becomes more difficult to detect outliers for values generated during the peak of the austral summer. A similar problem occurs at the lower end of the spectrum when the envelope is very narrow. Differences between very small values can fall outside of the confidence interval. These values have little impact on the model so their removal is generally not necessary. These records, however, appear as outliers and may obscure real anomalies.

APPENDIX B (continued)

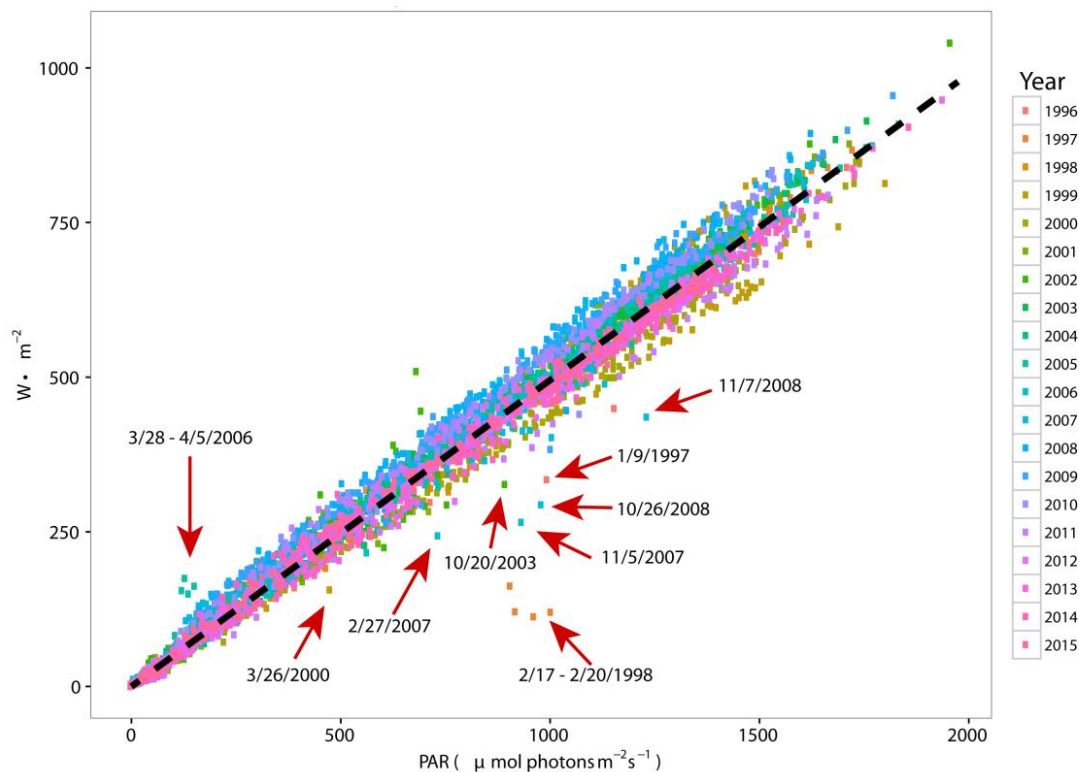


Fig. 4, Appendix B. PAR plotted against SWR observations from Lake Fryxell met station. Statistical anomalies that plot above the linear regression indicate anomalies with PAR values. Values that plot below the line are SWR anomalies.

The third method used to identify anomalies in the meteorological record was to plot PAR normalized by SWR as a time series. This approach takes advantage of the tight correlation between the two signals to identify anomalous data during the peak of the austral summer. Plotting these data by year helps identify periods in the record of any length of time that diverge from the rest of the record. The range of normalized values is greatest at the beginning (Aug/Sep) and end of the austral summer (Apr/May) and smaller during the height of summer (**Fig. 5**, Appendix B). Anomalies in this visualization method appear as spikes or troughs in the time series. One such example was identified in the Lake Bonney record where a period between November and January of the 2001/2002 field season appears separate from the rest of the data. Cross examination against the time series facet plots for this period suggest an under-response of

APPENDIX B (continued)

the PAR sensor. Since the anomaly occurred at the height of summer when the confidence interval was largest it was not identified as a statistical outlier.

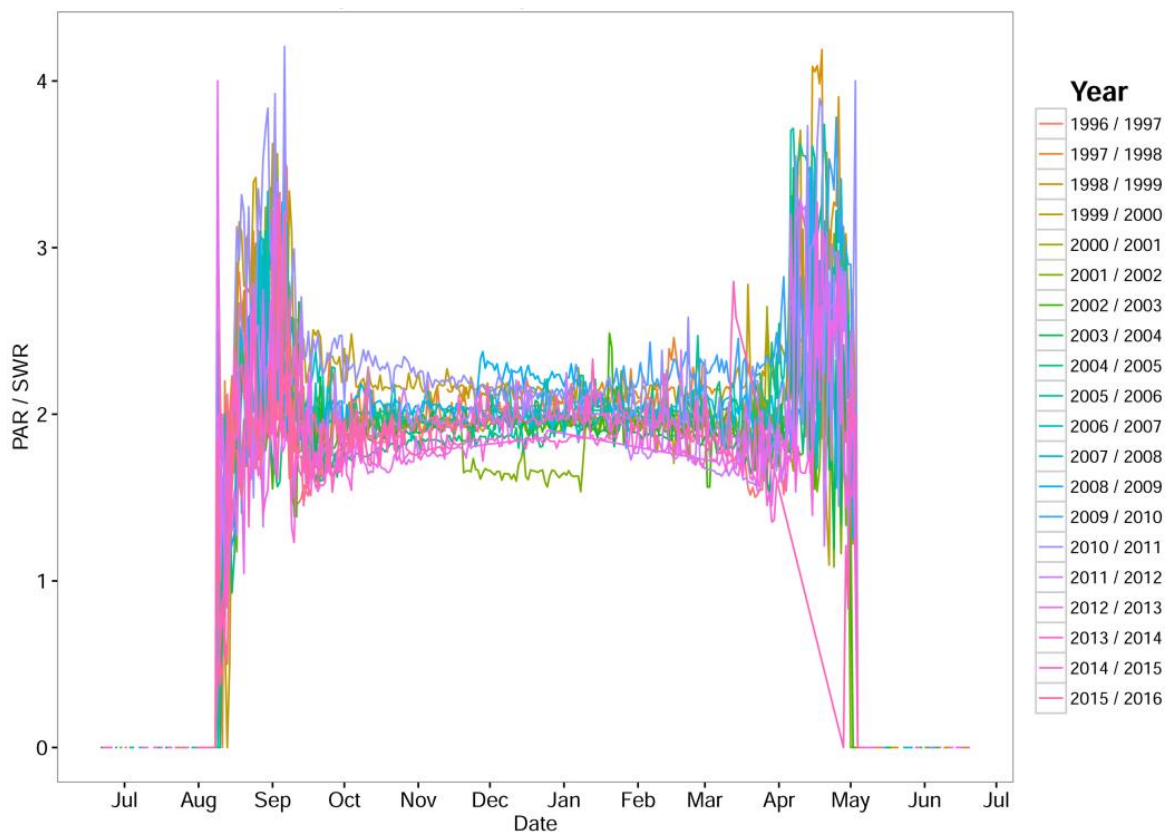


Fig. 5, Appendix B. Daily PAR normalized by SWR for all seasons on record from Lake Bonney met. This method of visualization helps identify anomalies in the record that can be overlooked by other methods.

CITED LITERATURE

- AGUILAR, C., HERRERO, J. & POLO, M.J. 2010. Topographic effects on solar radiation distribution in mountainous watersheds and their influence on reference evapotranspiration estimates at watershed scale. *Hydrology and Earth System Sciences*, **14**, 2479–2494, 10.5194/hess-14-2479-2010.
- BIELEWICZ, S., BELL, E., KONG, W., FRIEDBERG, I., PRISCU, J.C. & MORGAN-KISS, R.M. 2011. Protist diversity in a permanently ice-covered Antarctic Lake during the polar night transition. *The ISME journal*, **5**, 1559–1564, 10.1038/ismej.2011.23.
- CHINN, T.J. 1993. Physical hydrology of the dry valley lakes. *Physical and Biogeochemical processes in Antarctic Lakes. Antarctic Research Series*, **59**, 1–51.
- CLEVELAND, W.S. & DEVLIN, S.J. 1988. Locally Weighted Regression: An Approach to Regression Analysis by Local Fitting. *Journal of the American Statistical Association*, **83**, 596, 10.2307/2289282.
- DANA, G.L., WHARTON, R.A.J. & DUBAYAH, R. 1998. Solar radiation in the McMurdo Dry valleys, Antarctica. *Ecosystem Dynamics in a Polar Desert: the McMurdo Dry Valleys, Antarctica. Antarctic Research Series*, **72**, 39–65.
- DANA, G.L., WHARTON, R.A.J. & FOUNTAIN, A.G. 1996. McMurdo Dry Valleys LTER: Solar radiation on glaciers in Taylor Valley, Antarctica. *Antarctic Journal*, 191–193.
- DHAULAKHANDI, A.B., JOSHI, R.P. & JOSHI, M.C. 1993. Availability of Photosynthetically Active Radiation in Antarctica. *Current Science*, **65**, 703–705.
- DORAN, P.T., DANA, G.L., HASTINGS, J.T. & WHARTON, R.A.J. 1995. McMurdo Dry Valleys Long-Term Ecological Research (LTER) LTER automatic weather network (LAWN). *Antarctic Journal*, 276–280.
- DORAN, P.T., MCKAY, C.P., CLOW, G.D., DANA, G.L., FOUNTAIN, A.G., NYLEN, T.H. & LYONS, W.B. 2002. Valley floor climate observations from the McMurdo dry valleys, Antarctica, 1986–2000. *Journal of Geophysical Research*, **107**, ACL 13–1 – 12, 10.1029/2001JD002045.
- DORAN, P.T., MCKAY, C.P., FOUNTAIN, A.G., NYLEN, T.H., MCKNIGHT, D.M., JAROS, C. & BARRETT, J.E. 2008. Hydrologic response to extreme warm and cold summers in the McMurdo Dry Valleys, East Antarctica. *Antarctic Science*, **20**, 499–509, 10.1017/S0954102008001272.

- DORAN, P.T., WHARTON, R.A.J. & LYONS, W.B. 1994. Paleolimnology of the McMurdo Dry Valleys, Antarctica. *Journal of Paleolimnology*, **10**, 85–114.
- DOZIER, J. 1980. A Clear-Sky Spectral Solar Radiation Model for Snow-Covered Mountainous Terrain. *Water Resources Research*, **16**, 709–718.
- DUBAYAH, R. & LOECHEL, S. 1997. Modeling Topographic Solar Radiation Using GOES Data. *Journal of Applied Meteorology and Climatology*, **36**, 141–154.
- DUBAYAH, R. & RICH, P.M. 1995. Topographic solar radiation models for GIS. *International journal of geographical information systems*, **9**, 405–419, 10.1080/02693799508902046.
- ESRI. 2015a. An overview of the Hydrology toolset. *ArcGIS 10.3.1 Help* Available at: <http://desktop.arcgis.com/en/arcmap/10.3/tools/spatial-analyst-toolbox/an-overview-of-the-hydrology-tools.htm> [Accessed June 4, 2015].
- ESRI. 2016. ArcGIS for Desktop Advanced Student Edition.
- ESRI. 2015b. How solar radiation is calculated. *ArcGIS 10.3.1 Help* Available at: <http://desktop.arcgis.com/en/arcmap/10.3/tools/spatial-analyst-toolbox/how-solar-radiation-is-calculated.htm> [Accessed June 4, 2015].
- ESRL - GMD. NOAA Solar Calculator. *Earth System Research Laboratory - Global Monitoring Division* Available at: <http://www.esrl.noaa.gov/gmd/grad/solcalc/>.
- FOUNTAIN, A.G., LYONS, W.B., BURKINS, M.B., DANA, G.L., DORAN, P.T., LEWIS, K.J., MCKNIGHT, D.M., et al. 1999. Physical Controls on the Taylor Valley Ecosystem, Antarctica. *BioScience*, **49**, 961–971.
- FOUNTAIN, A.G., NYLEN, T.H., MONAGHAN, A., BESAGIC, H. & BROMWICH, D.H. 2009. Snow in the McMurdo Dry Valleys, Antarctica. *International Journal of Climatology*, 10.1002/joc.
- HAWES, I., GILES, H. & DORAN, P.T. 2014. Estimating photosynthetic activity in microbial mats in an ice-covered Antarctic lake using automated oxygen microelectrode profiling and variable chlorophyll fluorescence. **59**, 674–688, 10.4319/lo.2014.59.3.0674.
- HOFFMAN, M.J., FOUNTAIN, A.G. & LISTON, G.E. 2008. Surface energy balance and melt thresholds over 11 years at Taylor Glacier, Antarctica. *Journal of Geophysical Research F: Earth Surface*, **113**, F04014, 10.1029/2008JF001029.
- JENKINS, A. 2013. The Sun's position in the sky. *European Journal of Physics*, **34**, 633–652, 10.1088/0143-0807/34/3/633.

- KATURJI, M., ZAWAR-REZA, P. & ZHONG, S. 2013. Surface layer response to topographic solar shading in Antarctica's dry valleys. *Journal of Geophysical Research: Atmospheres*, **118**, 12,332–12,344, 10.1002/2013JD020530.
- KENNEDY, A.D. 1993. Water as a limiting factor in the Antarctic terrestrial environment: A biogeographical synthesis. *Arctic and Alpine Research*, 308–315.
- KOCH, S.E., DESJARDINS, M. & KOCIN, P.J. 1983. An interactive Barnes objective map analysis scheme for use with satellite and conventional data. *Journal of Climate and Applied Meteorology*, **22**, 1487–1503, 10.1175/1520-0450(1983)022<1487:AIBOMA>2.0.CO;2.
- KUIPERS MUNNEKE, P., REIJMER, C.H. & VAN DEN BROEKE, M.R. 2011. Assessing the retrieval of cloud properties from radiation measurements over snow and ice. *International Journal of Climatology*, **31**, 756–769, 10.1002/joc.2114.
- LANDSAT 8. 2014. LC80561162014353LGN00 - 2014-12-19/15.00%/74.49°. *Libra DevelopmentSEED* Available at: <https://libra.developmentseed.org/> [Accessed January 1, 2015].
- LEVY, J. 2013. How big are the McMurdo Dry Valleys? Estimating ice-free area using Landsat image data. *Antarctic Science*, **25**, 119–120, 10.1017/S0954102012000727.
- LISTON, G.E. & ELDER, K. 2006. A Meteorological Distribution System for High-Resolution Terrestrial Modeling (MicroMet). *Journal of Hydrometeorology*, **7**, 217–234.
- LIU, B.Y.H. & JORDAN, R.C. 1960. The interrelationship and characteristic distribution of direct, diffuse and total solar radiation. *Solar Energy*, **4**, 1–19, 10.1016/0038-092X(60)90062-1.
- LTER. 2014. MCMLTER Met Station Measurement Intervals and Samping Frequency, 1-6 pp. Available at: http://www.mcmlter.org/queries/met/met_home.jsp#browse.
- LUTGENS, F.K., TARBUCK, E.J. & TASA, D. 2012. Chapter 20: Global Climate Change. *In Essentials of Geology*. 502–509.
- LYONS, W.B., FOUNTAIN, A., DORAN, P., PRISCU, J.C., NEUMANN, K. & WELCH, K. A. 2000. Importance of landscape position and legacy: The evolution of the lakes in Taylor Valley, Antarctica. *Freshwater Biology*, **43**, 355–367, 10.1046/j.1365-2427.2000.00513.x.
- LYONS, W.B., FRAPE, S.K. & WELCH, K.A. 1999. History of McMurdo Dry Valley lakes, Antarctica, from stable chlorine data. *Geology*, **27**, 527–530.
- LYONS, W.B., WELCH, K.A., SNYDER, G., OLESIK, J., GRAHAM, E.Y., MARION, G.M. &

- POREDA, R.J. 2005. Halogen geochemistry of the McMurdo Dry Valleys lakes, Antarctica: Clues to the origin of solutes and lake evolution. *Geochimica et Cosmochimica Acta*, **69**, 305–323, 10.1016/j.gca.2004.06.040.
- MCGINNIS, L.D., NAKAO, K. & CLARK, C.C. 1973. Geophysical Identification of Frozen and Unfrozen Ground Antarctica. *In Permafrost North American Contribution Second International Conference*. Washington DC, USA: National Academy of Sciences, 136–146.
- MEYERS, T.P. & DALE, R.F. 1983. Predicting Daily Insolation with Hourly Cloud Height and Coverage. *Journal of Applied Meteorology and Climatology*, **22**, 537–545.
- MICHALSKY, J.J. 1988. The Astronomical Almanac's algorithm for approximate solar position (1950-2050). *Solar Energy*, **40**, 227–235, 10.1016/0038-092X(88)90045-X.
- MIZOGUCHI, Y., YASUDA, Y., OHTANI, Y., WATANABE, T., KOMINAMI, Y. & YAMANOI, K. 2013. A practical model to estimate photosynthetically active radiation using general meteorological elements in a temperate humid area and comparison among models. *Theoretical and Applied Climatology*, **115**, 583–589, 10.1007/s00704-013-0912-2.
- NYLEN, T.H., FOUNTAIN, A.G. & DORAN, P.T. 2004. Climatology of katabatic winds in the McMurdo Dry Valleys, southern Victoria Land, Antarctica. *Journal of Geophysical Research*, **109**.
- OBRYK, M.K., DORAN, P.T. & PRISCU, J.C. 2014. Journal of Geophysical Research: Biogeosciences. *The permanent ice cover of Lake Bonney, Antarctica: The influence of thickness and sediment distribution on photosynthetically available radiation and chlorophyll-a distribution in the underlying water column*, 557–566, 10.1002/2013JG002433.
- ORGILL, J.F. & HOLLANDS, K.G.T. 1977. Correlation equation for hourly diffuse radiation on a horizontal surface. *Solar Energy*, **19**, 357–359, 10.1016/0038-092X(77)90006-8.
- POAGE, M.A., BARRETT, J.E., VIRGINIA, R.A. & WALL, D.H. 2008. The Influence of Soil Geochemistry on Nematode Distribution, Mcmurdo Dry Valleys, Antarctica. *Arctic, Antarctic, and Alpine Research*, **40**, 119–128, 10.1657/1523-0430(06-051).
- PONS, X. & NINYEROLA, M. 2008. Mapping a topographic global solar radiation model implemented in a GIS and refined with ground data. *International Journal of Climatology*, **28**, 1821–1834, 10.1002/joc.
- R CORE TEAM. 2014. R: A language and environment for statistical computing Available at: <http://www.r-project.org/>.

- REDA, I. & ANDREAS, A. 2008. Solar Position Algorithm for Solar Radiation Applications (Revised), 1-56 pp, 10.1016/j.solener.2003.12.003.
- RSTUDIO TEAM. 2015. RStudio: Integrated Development for R Available at: <http://www.rstudio.com/>.
- RUIZ-ARIAS, J.A., ALSAMAMRA, H., TOVAR-PESCADOR, J. & POZO-VIZQUEZ, D. 2010. Proposal of a regressive model for the hourly diffuse solar radiation under all sky conditions. *Energy Conversion and Management*, **51**, 881–893, 10.1016/j.enconman.2009.11.024.
- SMITH, J.L., BARRETT, J.E., TUSNÁDY, G., REJTÖ, L. & CARY, S.C. 2010. Resolving environmental drivers of microbial community structure in Antarctic soils. *Antarctic Science*, **22**, 673–680, 10.1017/S0954102010000763.
- SPIGEL, R.H. & PRISCU, J.C. 1998. Physical limnology of the McMurdo Dry Valleys lakes. *Ecosystem Dynamics in a Polar Desert: the McMurdo Dry Valleys, Antarctica. Antarctic Research Series*, **72**, 153–187.
- WAGNER, B., ORTLEPP, S., DORAN, P.T., KENIG, F., MELLES, M. & BURKEMPER, A. 2011. The Holocene environmental history of Lake Hoare, Taylor Valley, Antarctica, reconstructed from sediment cores. *Antarctic Science*, **23**, 307–319, 10.1017/S0954102011000125.
- WENDLER, G. 1986. The “Radiation Paradox” on the Slopes of the Antarctic Continent. *Polarforschung*, **56**, 33–41.
- ZHANG, H., XIN, X., LI, L. & LIU, Q. 2013. An improved parametric model for simulating cloudy sky daily direct solar radiation on tilted surfaces. *IEEE Journal of Selected Topics in Applied Earth Observations and Remote Sensing*, **6**, 180–187, 10.1109/JSTARS.2012.2211000.

VITA

NAME: Dimitri Ricardo Acosta

EDUCATION: M.S., Earth and Environmental Science, University of Illinois at Chicago, Chicago, Illinois 2016

B.A., Anthropology/Psychology, Northwestern University, Evanston, Illinois 2005

TEACHING EXPERIENCE: Department of Earth and Environmental Science, University of Illinois at Chicago, Chicago, Illinois 2014 – 2016

ADDITIONAL RESEARCH EXPERIENCE: Physical Limnology and Meteorology of the McMurdo Dry Valleys, Antarctica, McMurdo Long-Term Ecological Research 2014 – 2016

HONORS: Beca al Extranjero, Consejo Nacional de Ciencia y Tecnología 2014-2016

Northwestern University Departmental Honors – Anthropology 2005

Northwestern University Department of Anthropology Research Grant 2004

Northwestern University Undergraduate Summer Research Grant 2004